In situ terminal settling velocity measurements at Stromboli volcano: Input from physical characterization of ash

V. Freret-Lorgeril[1], F. Donnadieu[1,2], J. Eychenne[1], C. Soriaux[1], T. Latchimy[2].

[1]*Université Clermont Auvergne, CNRS, IRD, OPGC, Laboratoire Magmas et Volcans, F-63000 Clermont-Ferrand, France*

[2]*CNRS, UMS 833, OPGC, Aubière, France*

Corresponding author: valentin.freretlo@gmail.com

ABSTRACT

Ash particle terminal settling velocity is an important parameter to measure in order to constrain the internal dynamics and dispersion of volcanic ash plumes and clouds that emplace ash fall deposits from which source eruption conditions are often inferred. Whereas the total Particle Size Distribution (PSD) is the main parameter to constrain terminal velocities, many studies have empirically highlighted the need to consider shape descriptors such as the sphericity to refine ash settling velocity as a function of size. During radar remote sensing measurements of weak volcanic plumes erupted from Stromboli volcano in 2015, an optical disdrometer was used to measure the size and settling velocities of falling ash particles over time, while six ash fallout samples were collected at different distances from the vent. We focus on the implications of the physical parameters of ash for settling velocity measurements and modeling. Two-dimensional sizes and shapes are automatically characterized for a large number of ash particles using an optical morpho-grainsizer MORPHOLOGI G3. Manually sieved ash samples show sorted, relatively coarse PSDs spanning a few microns to 2000 µm with modal values between 180-355 µm. Although negligible in mass, a population of fine particles below 100 µm form a distinct PSD with a mode around 5-20 µm. All size distributions are offset compared to the indicated sieve limits. Accordingly, we use the diagonal of the upper mesh sizes as the upper sieve limit. Morphologically, particles show decreasing average form factors with increasing circle-equivalent diameter, the latter being equal to 0.92 times the average size between the length and intermediate axes of ash particles. Average particle densities measured by water pycnometry are 2755 ± 50 kg m^{-3} and increase slightly from 2645 to 2811 kg m^{-3} with decreasing particle size. The measured settling velocities under laboratory conditions with no wind, < 3.6 m s^{-1}, are in agreement with the field velocities expected for particles with sizes < 460 µm. The Ganser (1993) empirical model for particle settling velocity is the most consistent with our disdrometer settling velocity results. Converting disdrometer detected size into circle equivalent diameter shows similar PSDs between disdrometer measurements and G3 analyses. This validates volcanological applications of the disdrometer to monitor volcanic ash sizes and settling velocities in real-time with ideal field conditions. We discuss ideal conditions and the measurement limitations. In addition to providing sedimentation rates in-situ, calculated reflectivities can be compared with radar reflectivity measurements inside ash plumes to infer first-order ash plume concentrations. Detailed PSDs and shape parameters may be used to further refine radar-derived mass loading retrievals of the ash plumes.

Highlights:

- An optical disdrometer is used to measure ash sizes and settling velocities at Stromboli.
- Collected ash samples show sorted and coarse particle size distributions.
- Ash particles density and sphericity slightly decrease with augmenting size.
- Ganser's law (1993) best fits disdrometer field measurements of settling velocities.
- Volcanological applications of disdrometers to monitor ash fallout are validated.

Keywords: Terminal Settling Velocity; Ash fallout; Particle size; Morphology; Disdrometer; Stromboli.

1. Introduction

Constraining volcanic ash plume dynamics, dispersion and fallout processes is of paramount importance for the mitigation of related impacts, such as those on infrastructure, transportation networks, human health (Baxter, 1999; Wilson *et al.*, 2009; Wilson *et al.*, 2012). The terminal settling velocity (V_T) of particles transported in volcanic ash plumes influences plume dispersal in the atmosphere, controls the sedimentation pattern in space and time, and in turn, the formation of ash deposits (Beckett *et al.*, 2015; Bagheri & Bonadonna, 2016a). V_T is used to estimate ash mass deposition rates (Pfeiffer *et al.*, 2005; Beckett *et al.*, 2015) and it mainly depends on the total grain size distribution (TGSD), and the density and the shape of ash particles. Retrieving the TGSD in real-time is currently impossible for operational purpose owing to the lack of direct measurements of the *in situ* Particle Size Distribution (PSD; *e.g.*, inside the plume). It is generally obtained from post-eruption analyses of ash deposits (Andronico *et al.*, 2014) or from a multi-sensor strategy (Bonadonna *et al.*, 2011; Corradini *et al.*, 2016) comprising, for instance, satellite images (Prata, 1989; Prata & Grant, 2001; Prata & Bernardo, 2009) and radar remote sensing (Marzano *et al.*, 2006a, 2006b), coupled to ground sampling. Meteorological optical disdrometers, although originally designed for hydrometeors, can be used to record volcanic ash fallout, and provide particle number density, settling velocities and sizes in near real-time at a single location. Disdrometer measurements can be used to calibrate dispersion model outputs, as well as radar observations from an empirical law relating derived radar reflectivity factors and associated particle mass concentrations. First-order estimates of their mass loading parameters, of primary importance for hazard evaluation, can then be made by comparing the calculated reflectivities to radar measurements inside ash plumes (Maki *et al.*, 2016).

Volcanic Ash Transport and Dispersion (VATD) models require equations relating V_T to particle size distribution in order to make accurate forecasts of ash dispersion and deposition. As V_T also depends on particle shape parameters and densities, these need to be characterized as a function of sizes. Ash particles are highly heterogeneous in shape and size due to a variety of fragmentation processes (Cashman & Rust, 2016), leading to the development of empirical laws describing the aerodynamic drag of the particles, from which terminal velocity depends. Initially this was done for spherical grains (Gunn & Kinzer, 1947; Wilson & Huang, 1979 and references therein) and then for non-spherical particle shapes based on laboratory experiments

(Kunii & Levenspiel, 1969; Ganser, 1993; Chien, 1994; Dellino *et al.*, 2005; Coltelli *et al.*, 2008; Dioguardi & Mele, 2015; Bagheri & Bonadonna, 2016b; Del Bello *et al.* 2017; Dioguardi *et al.*, 2017). Such studies have revealed the need to consider the morphological aspects of ash particles to refine V_T estimates, in addition to the total grain size distribution.

A geophysical measurement campaign at Stromboli volcano was carried out between the 23rd of September and the 4th of October 2015 to characterize the mass load of ash plumes and their dynamics using radars at different wavelengths, including a millimeter-wave radar for ash tracking (Donnadieu *et al.*, 2016). In addition, falling ash particles were measured in-situ and in real-time using an optical disdrometer and samples from ground tarps, in order to constrain the PSD. The PSD is required to quantify the mass load parameters of the plume from the radar reflectivity measurements.

In this paper, we present a physical characterization of ash particles from Strombolian weak plumes using ash samples collected from ground tarps and near-ground disdrometer measurements of the falling ash. **Section 2** focuses on the instruments and methodologies utilized to characterize ash samples and these results are presented in **section 3**. In **section 4** we present V_T measurements of ash particles obtained in the field and under laboratory conditions and compare them to existing empirical models. We discuss the results and limitations and then give conclusive remarks of this study in **section 5** and **6**, respectively.

2. Materials and methods

2.1 Ash sampling in the field

Ash samples from ash-laden plumes of Stromboli volcano were collected on the ground from a 0.4 m^2 tarp (0.45 m × 0.9 m) and a collector (0.6 m × 0.6 m) during a Doppler radar measurement campaign between the 23rd September and the 4th October 2015 (Donnadieu *et al.*, 2016). During this period, Stromboli eruptive activity was weak, producing type 2a and/or 2b eruptions (Patrick *et al.*, 2007), which are characterized by the emission of ash plumes rising 200 to 400 m high above the active vents, and drifted towards the North to the North-East with prevailing winds. Six ash samples from different ash fallout events were collected on a ground tarp at different locations and distances from the area of the craters: (i) two on the NE flank

(Roccete) 500 to 600 m from the summit vents (white cross in **Figure 1**), (ii) three near Pizzo Sopra la Fossa, ~320-330 m northeast of the SW crater (blue cross in **Figure 1**), next to the optical disdrometer (white square in **Figure 1**), and (iii) one in a collector at Punta Labronzo ~2 km to the North (green cross in **Figure 1**). Details on ash sample collection dates and locations are summarized in **Table 1**.

Table 1*: Date and locations of the six collected ash samples.*

Date (mm/dd/yyyy)	Eruption time UTC (HH:MM)	location	Sample names	GPS point (UTM)	Collected mass (g)
09/25/2015	16:36	near Pizzo Sopra la Fossa	1636_summit	33 S 0518663 UTM 4293821	0.642
10/02/2015	12:46	NE flank (Roccete)	1246_roc	33 S 0518774 UTM 4294327	4.971
10/02/2015	15:30	Punta Labronzo	1530PL	33 S 0518720 UTM 4295743	0.259
10/02/2015	15:50	near Pizzo Sopra la Fossa	1550_summit	33 S 0518663 UTM 4293821	0.068
10/03/2015	10:42-12:52	NE flank (Roccete)	1042-1252_roc	33 S 0518774 UTM 4294327	6.801
10/03/2015	16:01	near Pizzo Sopra la Fossa	1601_summit	33 S 0518663 UTM 4293821	25.230

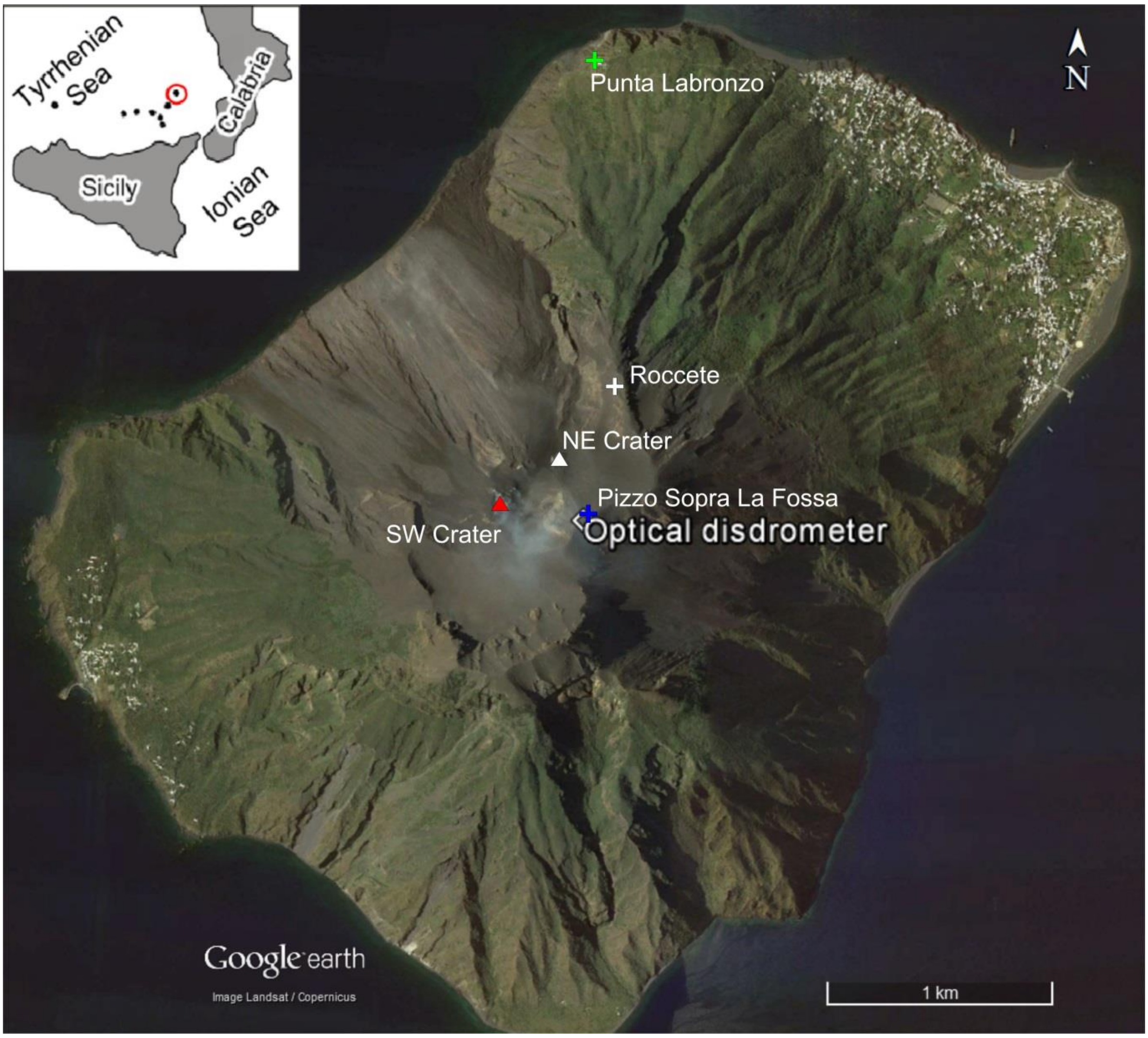

Figure 1*: Map of Stromboli Island. The Optical disdrometer was set up next to Pizzo Sopra la Fossa at 900 m a.s.l. (white square), 320 m and 330 m away from the NE (white triangle) and the SW crater (red triangle), respectively. Ash samples were collected at Pizzo Sopra la Fossa next to the disdrometer (blue cross), on the NE flank (Roccete) 500-670 m NE from the vents (white cross) and at Punta Labronzo (1530PL sample, green cross) about 2 km North from the vents.*

2.2 Grain-size and morphological analyses

The samples were manually sieved twice to determine their PSDs at 1/2 Φ and 1/4 Φ intervals. The mass of each fraction was measured with a 10^{-4} g accuracy weighing scale. The relation between Φ scale and circle equivalent diameters (D) is given by $\Phi = -\log_2(D\ (\mathrm{mm}))$. In total, less than 0.5% of the mass of ash collected was lost during the 1/2 Φ mechanical sieving. We calculated the sorting coefficient S_0 from Folk & Ward (1957):

$$S_0 = \frac{\Phi 84 - \Phi 16}{4} + \frac{\Phi 95 - \Phi 5}{6.6}, \qquad (1)$$

with Φ84, Φ16, Φ95 and Φ5 being the Φ values corresponding to the 84th, the 16th, the 95th and the 5th percentiles, respectively, of the calculated PSD. The lower the S_0, the more sorted the PSD.

To study the size and shapes of ash particles, we use the MORPHOLOGI G3^{TM} automated optical analyzer (named G3 is this study) designed by Malvern Instruments^{TM}. Particles from a given sieve are placed on a glass plate and illuminated from below (diascopic illumination). The G3's microscope measures the 2-D projected areas and shapes of a sample of particles, allowing an automatic analysis of morphological parameters such as the size and 2-D shape parameters. We used a × 5 magnification leading to an image resolution of 3.3 pixel/μm^2 (*i.e.* less than 0.5 μm of minimum resolution). Typically, tens of particles of size 1 Φ up to 18000 particles of size < 4 Φ can be processed in 35 minutes (fast and routine analyzes, Leibrandt & Le Pennec, 2015). In order to reduce the size range of the individual particles analyzed while keeping them optically focused, the half- Φ fractions were sieved at a 1/4 Φ. Obtained sieving results are presented in **Appendix A**.

We measure the following size parameters: (i) the longest axis (L) and (ii) intermediate axis (I) in the 2-D plane orthogonal to the light direction; (iii) the circle-equivalent diameter $D_{CE} = 2 \times (A_p/\pi)^{1/2}$ measured from the particle section area A_p; and (iv) the sphere-equivalent volume calculated with diameter D_{CE}. Due to the 2-D imaging inherent to the methodology, we assume that particles always show the maximum projection area (Bagheri & Bonadonna, 2016) and, hence, their short (S) axes are always oriented orthogonal to the image plan, *i.e.* $S \leq I$.

From the measurements of L, I and A_p, the following morphological parameters are defined: (i) the Elongation $e = I/L$ (Bagheri & Bonadonna, 2016b); (ii) the Convexity $C_v = P_{CH}/P_p$, corresponding to the textural roundness of the particles with perimeter P_p (Liu *et al.*, 2015), and P_{CH} being the convex hull perimeter (*i.e.* the smallest convex polygon containing all pixels of the analyzed particle); (iii) the solidity $S_d = A_p/A_{CH}$ (Cioni *et al.*, 2014), indicative of the high wavelength (*i.e.*, morphological) roughness of the particles (Cioni *et al.*, 2014; Liu *et al.*, 2015b) with A_{CH} being the convex hull area; and (iv) the sphericity $\varphi = 4\pi A_p/P_p^2$ as an indicator of the roughness and the shape of the particles (Riley *et al.*, 2003). The sphericity φ is equal to the square of the circularity C_c (*i.e.* equal to $2(\pi A_p)^{1/2}/P_p$) defined by Leibrandt & Le Pennec (2015). According to Liu *et al.* (2015a), the shape parameters associated to the convex hull, such as S_d and C_v, characterize the roughness of particles independently of their form.

These parameters range from 0 to 1 (*e.g.*, a perfect sphere has a value of 1) and are all described in Leibrandt & Le Pennec (2015), Liu *et al.* (2015a, 2015b) and Riley *et al.* (2003).

A complete PSD from G3 analyses, comprising all analyzed 1/4 Φ sieved fractions, is estimated by combining (i) the measured mass fractions from 1/4 Φ sieving with (ii) the sphere-equivalent volume (V_{SE}) of particles measured by the G3 for each analyzed fraction:

$$m_i^{wt\%} = \sum_j \left(\frac{\mathrm{V}_{SE\,i,j}}{\sum_i \left(\mathrm{V}_{SE\,i,j}\right)} m_j^{wt\%} \right), \tag{2}$$

where subscript i denotes the size bin containing individual particles analyzed by the G3 having a D_{CE} diameter within the upper and lower bounds of the bin, whereas subscript j stands for the sieve size fraction from manual sieving. Each bin i has a 5 µm resolution and the uncertainty associated with the G3 image resolution is thus considered as negligible. $m_i^{wt\%}$ is the weight fraction of particles in the ith bin size, and $m_j^{wt\%}$ is the mass percentage of the analyzed sieve fraction j of the total sample mass. The ratio $V_{SE\,i,j} / \sum_i \left(\mathrm{V}_{SE\,i,j}\right)$ is the sphere-equivalent volume ratio of particles belonging to the ith bin size with respect to all particles from a sieved fraction j. We use the sphere-equivalent volume derived from the G3, rather than the number of particles, to minimize the error propagation in the mass calculation due to the large increase in particle number with decreasing size.

2.3 Ash density measurements

The average densities of ash particles of 1/4 Φ sieved fractions of the two samples with the largest mass (1601_summit and 1246_roc) are measured by water pycnometry (Eychenne & Le Pennec, 2012). This method allows the estimation of ash particle density by volume difference between a 9.5×10^{-6} m^3 boro-silicate pycnometer filled with distilled and degassed water and then filled with water and a known mass of ash sample.

The density of particles is given by:

$$\rho_i = \frac{m_i \rho_w}{m_{w1} - m_{w2}}, \tag{3}$$

with ρ_i the density of the ith ash size class in kg.m^{-3}, ρ_w the density taken to be 1000 kg m^{-3}, m_i the mass of ash incorporated into the pycnometer (0.4 to 2 g), m_{w1} the mass of water required to fill the reference pycnometer volume and m_{w2} the mass of water required to fill the pycnometer once the ash sample has been added.

By using water pycnometry, we measure the average particle density of a given sieved fraction. For particles between 125 µm and 700 µm, we assume that water surface tension can be considered as sufficiently strong to avoid vesicle and asperity filling. For this hypothesis to be verified, the particles are dried in an oven before being incorporated into the water (Eychenne & Le Pennec, 2012). Thus, the measured densities correspond to the apparent densities of the particles, which represents their mass divided by their solid volume and the volume linked to their porosity.

2.4 The optical disdrometer and particle settling experiments

The optical disdrometer Parsivel^2, designed by OTT, uses a 780 nm wavelength laser beam emitted from a transmitter to a receiver, which converts the transmitted laser light into a voltage signal. Described in Löffler-Mang & Jürg (2000) and Tokay *et al.* (2014), the disdrometer measures the settling velocities and sizes of particles when as they pass through the laser sheet. The laser obscuration time is used to estimate the settling velocities. The longer a particle takes to cross the beam, the lower the settling velocity. Then, the amplitude of the laser light extinction is used to calculate the size of the particles. By measuring the number of falling particles and their settling velocity class values (**Appendix B**), the disdrometer calculates the number density of particles crossing the beam as:

$$N_i(D_i) = \frac{n_i}{v_i A \Delta t \mathrm{d}D_i}, \qquad (4)$$

with $N_i(D_i)$ the particle number density (mm^{-1} m^{-3}) of the ith disdrometer size class, n_i the number of detected particles with measured settling velocity v_i (m s^{-1}), A the laser sheet area (54×10^{-4} m^2), Δt the sampling interval (10 s) and dD_i the size range (mm) of the disdrometer ith size class. The disdrometer measures settling velocities between 0.05 and 20.8 m s^{-1} distributed among 32 classes (Classes 1 to 22 are displayed in **Appendix B**) and detects particles with diameter from 250 µm to 26×10^3 µm.

We performed in-situ measurements of falling ash during the field campaign at Stromboli. The disdrometer was set up about 80 cm above the ground close to Pizzo Sopra La Fossa (**Figure 1**), 320-330 m northeast of the SW crater. The disdrometer recorded the ash fallout events from weak Strombolian plumes that produced the two ash samples collected from ground tarps next to the disdrometer (1601_summit) and lower down the NE flank (1246_roc).

In order to establish the ash fallout detection limits of the disdrometer and to estimate the influence of the wind on particle settling velocities in the field, disdrometer retrievals are tested under laboratory conditions of no horizontal nor vertical wind. Sieved ash particles from the 1601_summit sample are dropped from heights between 3 m and 11 m above the disdrometer laser sheet in order to verify that terminal settling velocities were reached for each sieved size fraction.

2.5 Terminal settling velocity models

The terminal settling velocity depends on the size, the shape and the density of falling particles that affect their drag forces and hence the flow regime adopted by the ambient carrier fluid. For individual particle settling, V_T is defined by the following equation (Wilson & Huang, 1979; Woods & Bursik, 1991; Sparks *et al.*, 1997):

$$V_T = \sqrt{D_{CE} \frac{4g(\rho - \rho_a)}{3\rho_a C_D}}, \quad (5)$$

where V_T is the terminal settling velocity of the particle (m s^{-1}), D_{CE} is the circle-equivalent diameter corresponding to the diameter of a circle (applicable to a sphere) with area measured by the G3 for each particle, g is the gravitational acceleration (m s^{-2}), ρ and ρ_a are the particle and air densities, respectively, in kg m^{-3}. Here, ρ_a is equal to 1.2 kg m^{-3} at a temperature of 15 °C at sea level (similar to laboratory conditions) and equals to 1.12 kg m^{-3} at 900 m a.s.l. (similar to field conditions). Finally, C_D is the drag coefficient and depends on the shapes of the settling particles and the Reynolds number Re, which describes the flow regime in which particles fall:

$$Re = \frac{V_T D \rho_a}{\mu}, \quad (6)$$

where V_T corresponds to the settling velocity of a particle within a non-moving ambient fluid (*i.e.* the air in this case) with a viscosity μ (Pa s) equals to 1.85×10^{-5} Pa s at a temperature of 15 °C at sea level (similar to laboratory conditions) and equals to 1.786×10^{-5} Pa at 900 m a.s.l. (similar to field conditions).

To verify that ash particles were falling at their V_T, we compared the disdrometer measurements with empirical V_T laws that are based on the following assumptions.

First, for particle Reynolds Number between 0.4 and 500 at an altitude of 5 km above sea level (a.s.l.) and assuming spherical particle diameters less than 1500 µm, V_T of a particle can be expressed as (Kunii & Levenspiel, 1969; Bonadonna *et al.*, 1998; Coltelli *et al.*, 2008):

$$V_T = D\left(\frac{4g^2\rho^2}{255\mu\rho_a}\right)^{\frac{1}{3}}, \tag{7}$$

Then, we compare our results with the models of Ganser (1993) and Bagheri & Bonadonna (2016b) based on **Equation 5**, which account for non-spherical particle shapes. In such a case, the drag equations are derived from empirical analyses of particle settling velocities and are not related to the same particle shape parameters.

In Ganser (1993), C_D is determined as follows:

$$C_D = \frac{24}{ReK_1K_2}\left[1 + 0.1118\left(ReK_1K_2\right)^{0.6567}\right] + \left(\frac{0.4305}{1 + \frac{3305}{ReK_1K_2}}\right). \tag{8}$$

K_1 and K_2 being the Stokes' shape factor and the Newton's shape factor, respectively:

$$K_1 = \left(\frac{1}{3} + \frac{2}{3}\varphi^{-\frac{1}{2}}\right)^{-1}, \tag{9}$$

$$K_2 = 10^{1.8148(-\log\varphi)^{0.5743}}, \tag{10}$$

where φ is the G3-derived sphericity (Riley *et al.*, 2003) of particles considered as isometric ($I = S$) and is the best shape parameter to be used in the Ganser model (Alfano *et al.*, 2011).

In Bagheri & Bonadonna (2016b), C_D is calculated as:

$$C_D = \frac{24k_S}{Re}\left[1+0.125\left(Re\frac{k_N}{k_S}\right)^{\frac{2}{3}}\right]+\left[\frac{0.46}{1+5330\left(Re\frac{k_N}{k_S}\right)}\right], \tag{11}$$

with k_S and k_N, being shape factors equal to:

$$k_S = (F_s^{1/3} + F_s^{-1/3})/2, \tag{12}$$

where $F_S = f\ e^{1.3}\left(\frac{D_{CE}{}^3}{L\ I\ S}\right)$ and $F_N = f^2\ e\left(\frac{D_{CE}{}^3}{L\ I\ S}\right)$

and

$$k_N = 10^{\alpha_2\left[-\log\left(F_N\right)\right]^{\beta_2}}, \tag{13}$$

where $\alpha_2 = 0.45 + 10/\exp(2.5\log\left(\rho/\rho_a\right)+30)$ and $\beta_2 = 1-37/\exp(3\log\left(\rho/\rho_a\right)+100)$

These shape factors depend on 3-D ash particle axes such as L, I, S and also the elongation (I/L) and flatness (S/I).

Because C_D, Re and V_T are dependent on each other, we use an iterative approach to determine the settling velocities with both aforementioned models. We initialize V_T using the Stokes law, where $V_T^{Stokes} = (g\ D_{CE}^2\ (\rho - \rho_a))/18\mu$, and then iteratively calculate Re, C_D, and V_T (**Equation 5**). The iterations are stopped when the velocity difference is less than 10^{-8}.

Finally, we calculate V_T using the Dellino *et al.* (2005) relationship:

$$V_T = \frac{1.2065\mu\left(D_{CE}{}^3 g\left(\rho-\rho_a\right)\rho\psi^{1.6}/\mu^2\right)}{D_{CE}\rho}, \tag{14}$$

where ψ is a shape factor defined as the ratio between the particle sphericity (Riley *et al.*, 2003) and $1/C_c$. Thus, the combination of **Equation 5** and the drag coefficient of spherical particles leads to the equation of Dellino *et al.* (2005), which does not depend on C_D and Re. **Equation 14** is only valid for Reynolds number > 60-100 (Dioguardi *et al.*, 2018).

Ash morphological parameters are required in order to compare models of V_T for non-spherical particles to ash settling velocities measured in the field or under laboratory conditions. These parameters are characterized in the following section for Strombolian ash.

3 Ash characteristics

3.1 Particle size distribution by mechanical sieving and morpho-grainsizer

Here we present sieving results obtained for the six ash samples. Values are available in **Appendix A**. The PSD from 1/2 Φ sieving for the proximal samples collected on the summit have modal values ranging from 125-180 μm (1550_summit) to 250-355 μm (1601_summit) (**Figure 2**). The same range of PSD modes is observed for the proximal samples collected lower down on the East flank at Roccete (1042-1252_roc and 1246_roc). The 1530PL sample collected 2 km to the North of the summit vent at Punta Labronzo shows a mode at 125-180 μm. Particle sizes range from < 63 μm to 1400 μm in 1246_roc and from < 63 μm to 2000 μm in 1601_summit (**Figure 2**). Therefore, there is no obvious correlation between sample location and PSD, an observation also made by Lautze *et al.* (2013) on ash samples from type 2 eruptions at Stromboli in 2009. Sorting coefficients S_0 of 0.27-0.47 indicate sorted PSDs for all ash samples from a single ash plume (**Figure 2**). The higher sorting coefficient S_0 of 0.75 for the 1042-1252_roc sample is due to the collection of a 2-hour long succession of fallout events with potentially variable PSDs, the sum of which leads to a less sorted PSD. We cannot exclude some dust contamination from this sample.

Following the 1/4 Φ sieving, the particle number frequency histogram of each sieved fraction is calculated from the G3 analyses. As observed by Leibrandt & Le Pennec, 2015, PSDs from the sieve fractions show a large offset toward D_{CE} values larger than the sieve mesh sizes. In particular, the modal D_{CE} can lay well beyond the sieve mesh limits as shown for the 1601_summit sample (fractions < 63 μm to 425-500 μm; **Figure 3**). For example, the 250-300 μm sieve fraction (red PSD in **Figure 3**) actually ranges between 248-551.78 μm in D_{CE}, with a mode at 350 μm, leading to 95.1% of the PSD lying above the upper sieve limit.

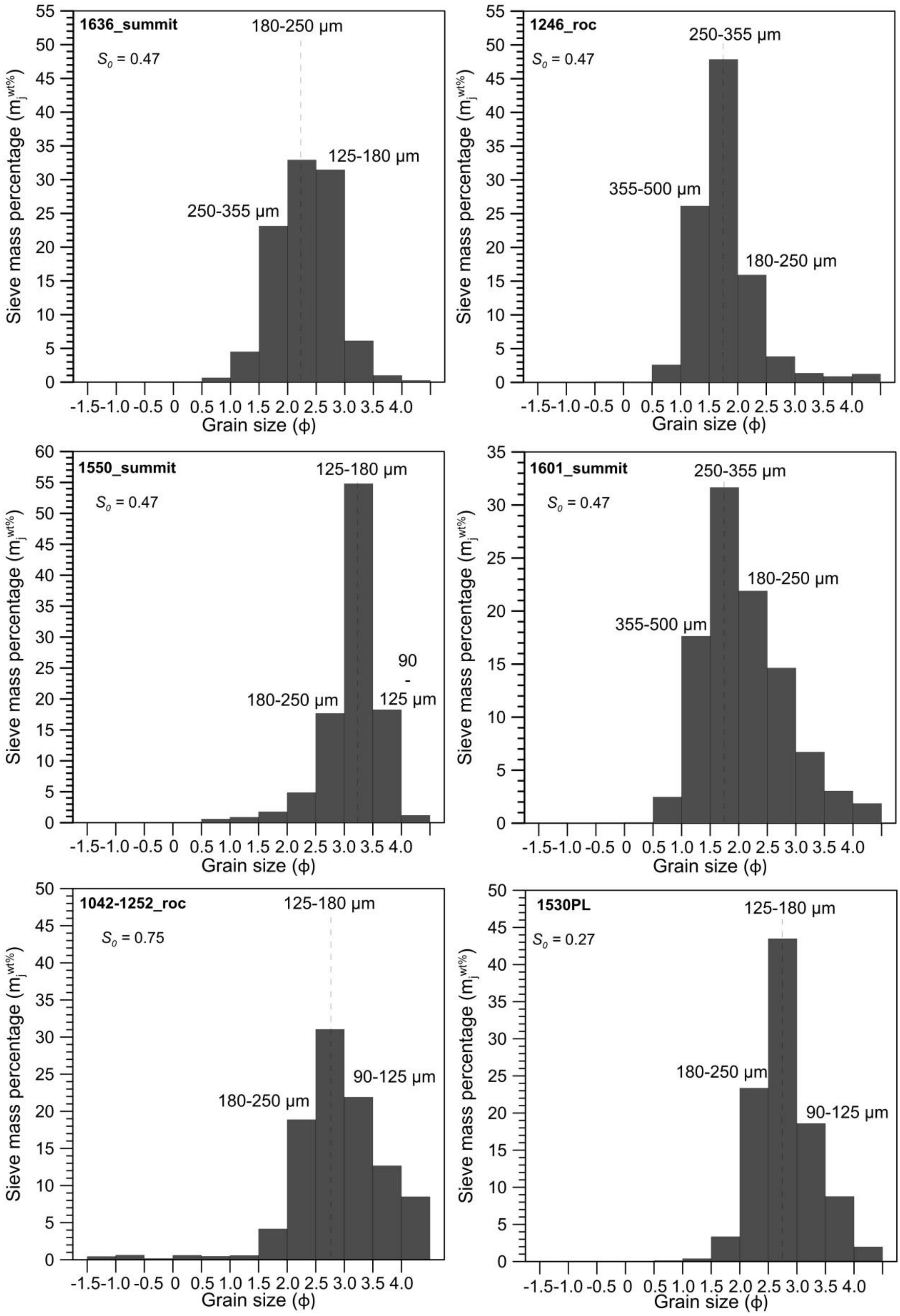

***Figure 2**: 1/2 Φ Particle size distributions determined by manual sieving for the six ash samples of Table 1. S_0 is the Folk & Ward (1957) sorting coefficient. Lower S_0 indicates better sorting.*

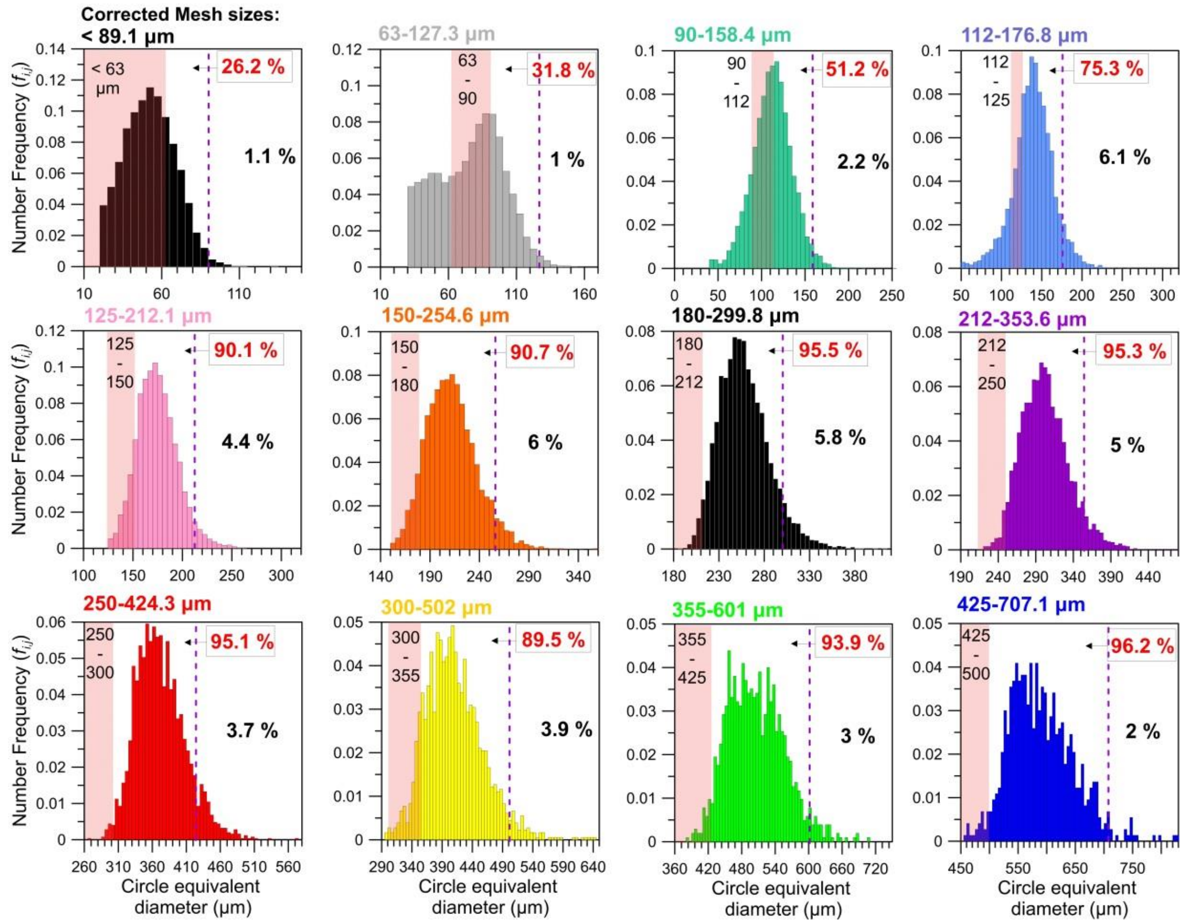

Figure 3: *Individual particle number frequency histograms retrieved from the G3 analyses of 1/4 Φ sieved fractions from the 1601_summit ash sample. Shaded red areas highlight the sieve intervals in circle-equivalent diameter and the percentage of the PSD larger than the upper sieve mesh is displayed in red. The vertical purple dashed lines indicate the diagonal dimension of the sieve upper mesh size, a better fit to the true PSD upper bound, as shown by the small residual percentage of the PSD (in black) larger than the diagonal of the sieve upper mesh. The intervals of the corrected sieve mesh sizes (down mesh size to diagonal of the upper mesh size) are indicated in color above each histogram.*

The number proportion of the PSD lying above the upper sieve limit increases with sieve mesh size, with a minimum value of 26.2% for the < 63 µm fraction and up to 96.2% for the 425-500 µm fraction. This discrepancy is explained by the fact that sieve mesh sizes (side dimension of the squared mesh) are given for supposedly spherical particles, whereas ash particles are non-spherical and often depart significantly from a spherical shape. Therefore, many particles with their largest and intermediate axes higher than the mesh size can be found in the sieved fraction depending on their orientation while passing through the mesh. The length of the squared mesh diagonal, as opposed to the mesh size, represents the true sieve upper limit when dealing with non-spherical particles, as shown by the small residual percentages of the PSD (1-6%) above the upper mesh diagonal length. Consequently, we use the lower mesh size and the diagonal length of the upper mesh, *i.e.* the upper mesh side length multiplied by √2 (vertical purple dashed line in **Figure 3**), to characterize the circle-equivalent diameter distributions of ash particles. These bounds of D_{CE} contain more than 94% of the ash particles in each fraction and are thus representative. In this new reference frame, for example, the 250-300 µm sieve fraction (*i.e.* $\Phi=2$) has D_{CE} lower and upper limits of 250 and 424.3 µm.

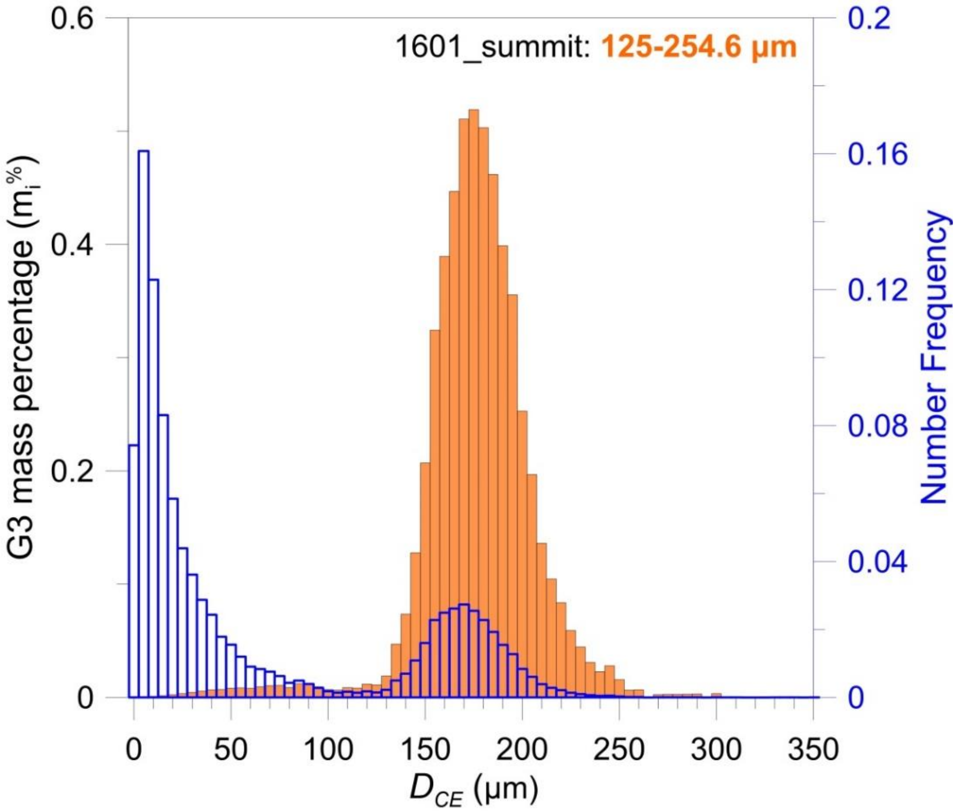

***Figure 4**: Comparison of mass- and number-based PSD in the 125-254.6 µm sieve fraction from the 1601_summit ash sample. The right axis represents the number frequency measured by G3 (blue histogram). The left axis represents the particle mass percentage $m_i^{\%}$ (orange bars) using sphere-equivalent volumes measured by the G3.*

Every sieved fraction of the six ash samples, when analyzed in number frequency, shows a distinct population of very fine ash particles with a relatively constant modal value between 5-20 µm. For example, in the 125-254.6 µm fraction of the 1601_summit sample (blue histogram in **Figure 4**), the secondary PSD of fine ash represents 73% of the total sieved fraction PSD in terms of particle number frequency (blue histogram in **Figure 4**), whereas these very fine particles represent only 3% of the whole PSD in mass or volume percentage. Likewise, in the other sieve fractions, the population of very fine ash appears as a decoupled PSD with a high contribution to the particle number frequency, but negligible in terms of mass or volume.

Finally, because D_{CE} distributions among successive sieve fractions exhibit a dramatic overlap (**Figure 3**), we calculate mass percentages (**Equation 2**) over the whole PSD in 5 µm bins by weighting the high resolution sphere-equivalent volume from the G3 analyses with the mass percentage of each sieved fraction at 1/4 Φ. This calculation leads to high resolution (5 µm) mass percentage PSDs for the six ash samples (**Figure 5**). They show a unimodal distribution whereas the 1/4 Φ sieves display two close maxima, the latter due to splitting of a unique mode at the bin transition (250 µm) into adjacent bins in **Figures 5A** and **5F**. For the 1601_summit and the 1042-1252_roc samples (**Figure 5A** and **Figure 5F**), the PSD obtained from the 1/2 Φ sieving broadly matches the corrected high resolution PSD in terms of modal value, whereas the 1/4 Φ PSDs tend to show a mode lower than that of the corrected PSD. Unlike the 1601_summit and 1042-1252_roc calculated PSD, the other calculated PSDs are well sorted (0.47-0.52).

The aforementioned artificial offset of the sieving PSDs toward smaller D_{CE} is more obvious in the other ash samples (**Figures 5B**, **5C**, **5D** and **5E**), emphasizing the significant bias on resulting PSD introduced by sieving non-spherical particles. Indeed, whereas spherical particles would be blocked by a sieve squared mesh having its side length corresponding to their diameter, coarser particles with some degree of elongation can cross the squared mesh along its diagonal (side length times $\sqrt{2}$) and appear in lower (smaller mesh-sized) sieves. As sieve mesh size intervals increase with diameter (*i.e.* decreasing Φ), the shift in diameter increases for coarser particles. Therefore, the sieving-derived PSDs agree more closely with high resolution PSDs derived from optical measurements for finer particles.

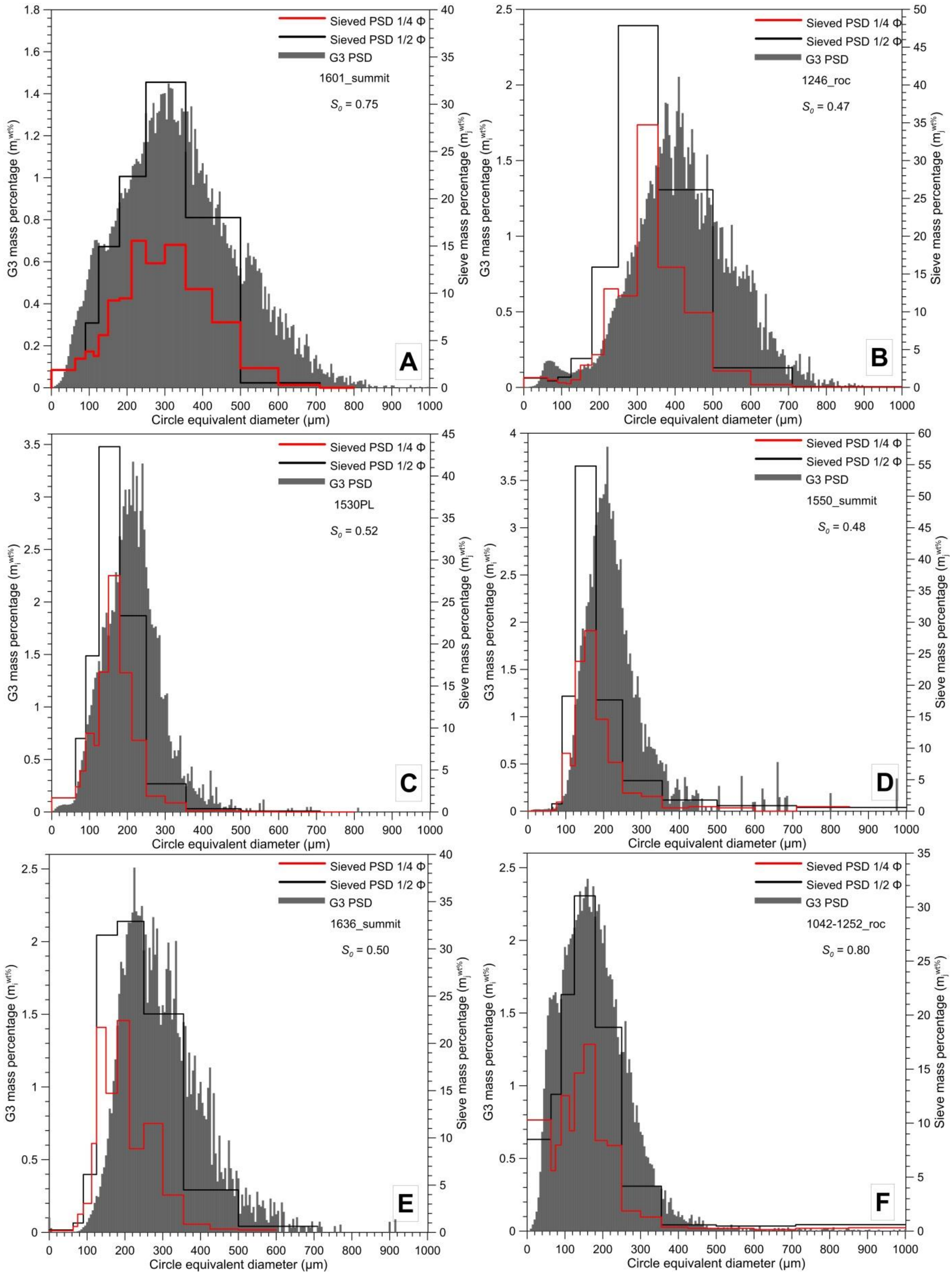

Figure 5: *Comparison of the PSDs calculated from G3 analyses with the PSDs inferred from manual sieving (1/4 Φ, red step line; 1/2 Φ, black step line) for the six ash samples 1601_summit **(A)**, 1246_roc **(B)**, 1530PL **(C)**, 1550_summit **(D)**, 1636_summit **(E)**, and 1042-1252_roc **(F)**.*

3.2 Ash densities

To constrain V_T, we use water pycnometry to measure the density of ash samples from the fallout detected by the optical disdrometer. Samples 1246_roc and 1601_summit have similar density trends (**Figure 6**). The average particle density of all measurements from the two summit samples is equal to 2755 ± 58 kg m^{-3}. The density trend beyond $\Phi \geq 2.5$ is uncertain because the measurement's accuracy is lower for fine particles and small sample mass, as seen from the increased spread of the 1601_summit measurements for $\Phi \geq 2.5$. For this reason, we mixed the 3.5 to 2.5 Φ fractions of the 1246_roc sample to calculate a more representative average density of 2811 ± 55 kg m^{-3}. In both samples, average densities slightly decrease with increasing diameter from Φ=2.5 to Φ=1 (*i.e.* 180-500 µm) from a maximum value of 2811 ± 55 kg m^{-3} to 2645 ± 35 kg m^{-3}. Over a particle size distribution, tephra densities typically form a sigmoidal trend that was previously described for andesitic, dacitic and rhyolitic ash (Eychenne & Le Pennec, 2012; Cashman & Rust, 2016). This sigmoidal trend is apparent for $\Phi \leq 0.5$ (*i.e.* $D_{CE} \geq 710$ µm) and the slight density decrease with increasing diameter might represent the beginning of a sigmoidal trend in density variation.

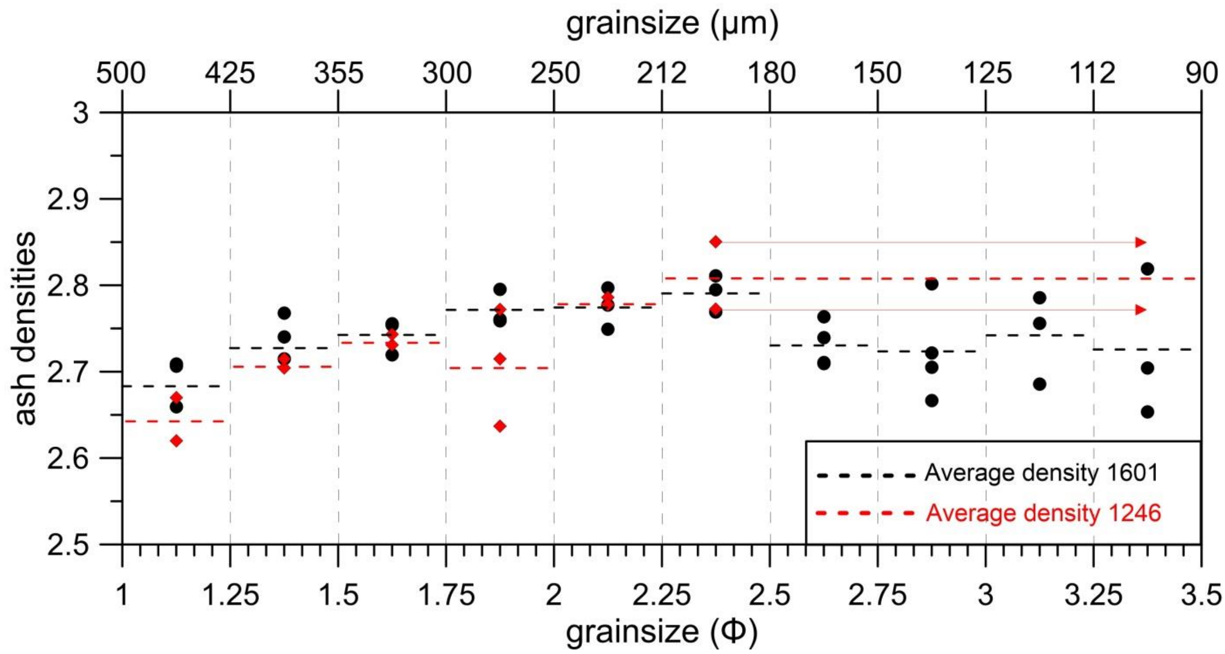

Figure 6*: Ash densities determined by water pycnometry for the two samples 1601_summit (grey dots) and 1246_roc (red diamonds) as a function of the 1/4 Φ fractions. Dashed lines correspond to the average density of each grain size class.*

3.3 Particle shapes

A comparison between S_d and C_v of the modal PSD classes of the six distinct ash samples (**Figures 2** and **5**) shows homogeneous average distributions of textural and morphological roughness among all samples (**Figure 7A** and **Table 2**). This observation is similar to morphometric analyses done by Lautze *et al.* (2011, 2013) at Stromboli showing no obvious relationship between particle shapes and the relatively short distance travelled from the source vent. In all samples, the average values of S_d and C_v are similar (**Table 2**) except for the 1042-1252_roc sample, which records several fallout events over a longer collection time, as opposed to the other samples, and is possibly contaminated by wind-drifted dust. Particles show high average solidity and convexity of 0.954 and 0.943, respectively (snapshot in **Figure 7A**).

Though rare, irregular shaped particles can be found in several samples. Such particles, characterized by the lowest values of C_v and S_d (*i.e.* 0.747 in sample 1530PL and 0.545 in sample 1246_roc), are displayed in **Figure 7A**. In total, and among all the samples, more than 90% of the analyzed particles show C_v and S_d values higher than 0.9, which characterize dense ash fragments (Liu *et al.*, 2015b).

Among the 6 samples, there is no clear systematic trend in sphericity as a function of particle size (**Figure 7B**). Sieved fraction average φ are within a narrow range between 0.7 and 0.92 (< 63 to 750 µm fractions) and decrease under 0.7 to minimum values of 0.5 in the 1530PL sample. Nevertheless, with respect to the standard deviation of sphericity in the 1601_summit sample, there is no significant variation of φ with D_{CE} up to 750 µm, beyond which values decrease slightly.

***Table 2**: Average Convexity C_v, Solidity S_d and Sphericity φ values of the modal sieved fractions (1/4 Φ) of the PSD for the six ash fallout samples.*

Sample names	Corrected Mesh (µm)	mean C_v	Standard deviation	Mean S_d	Standard deviation	mean φ	Standard deviation
1246_roc	300-502	0.956	± 0.020	0.947	± 0.027	0.770	± 0.067
1601_summit	300-502	0.945	± 0.020	0.947	± 0.026	0.765	± 0.068
1530PL	150-254.6	0.955	± 0.022	0.943	± 0.031	0.762	± 0.076
1550_summit	150-254.6	0.957	± 0.023	0.939	± 0.034	0.759	± 0.081
1636_summit	180-299.8	0.955	± 0.024	0.938	± 0.034	0.757	± 0.081
1042-1252_roc	150-254.6	0.921	± 0.032	0.927	± 0.033	0.707	± 0.081

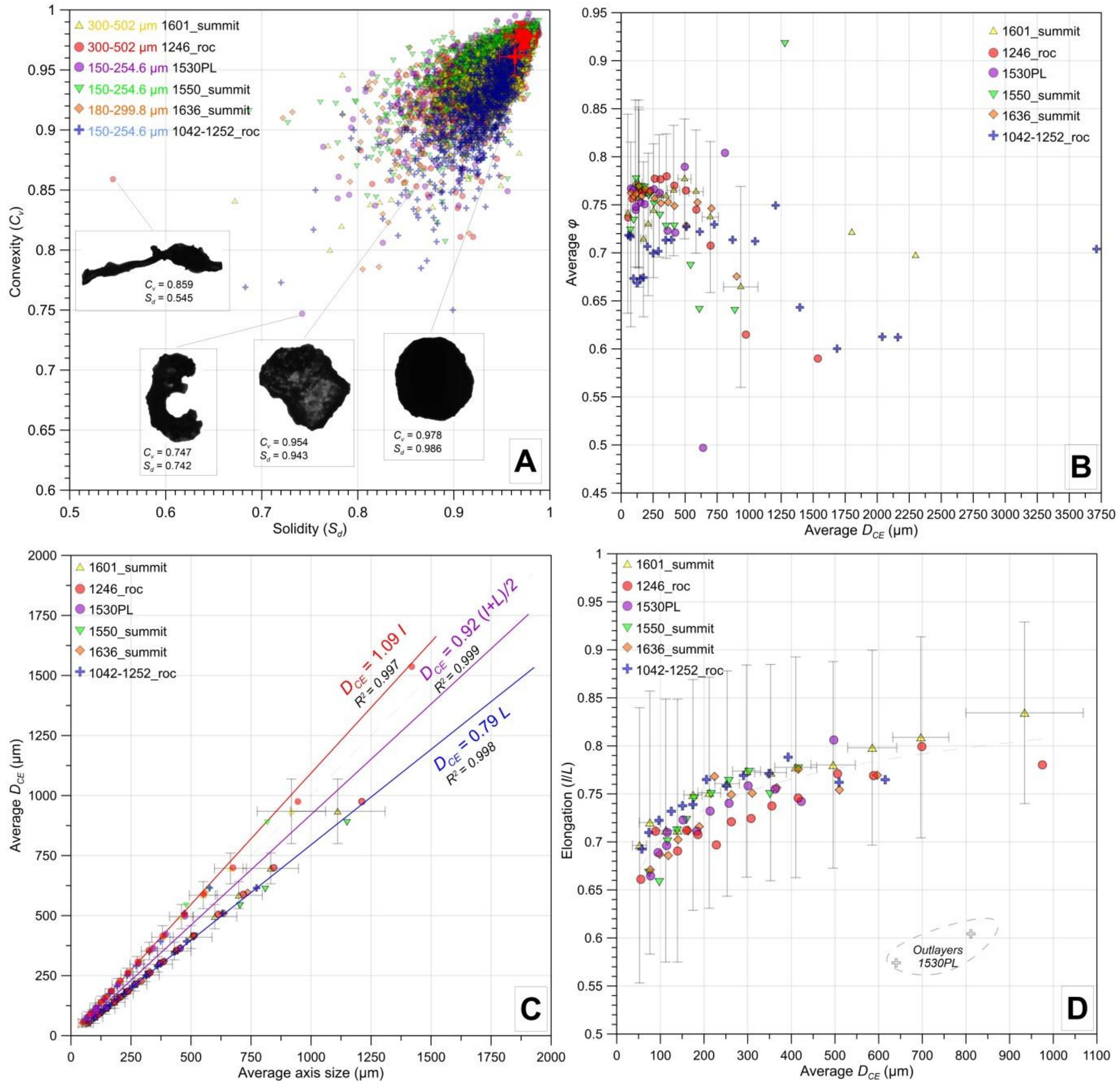

***Figure 7**: **A)** Clustergram of Convexity (C_v) as a function of the Solidity (S_d) of particles pertaining to the modal sieved fraction of the PSD for the 6 ash fallout samples. Average values of each population and their standard deviations are indicated in red bars and symbols. **B)** Average Sphericity (φ) of the sieved fractions as a function of their average circle-equivalent diameter (D_{CE}). **C)** Average Circle-equivalent diameter (D_{CE}) as a function of the average Length (L) and average Width (I). **D)** Average elongation (I/L) as a function of sieved fractions average D_{CE}. Errors bars (standard deviation) are shown in grey for the 1601_summit average values.*

The observation of particle shapes is essential to understand the measurements of the optical disdrometer in terms of V_T and sizes. Here, we assume that detected ash particles tend to fall perpendicularly to the plane defined by their maximum (*L*) and intermediate (*I*) axes (Bagheri & Bonadonna, 2016). Therefore, the disdrometer should measure sizes ranging between *L* and *I*, and an average value statistically approaching (*I*+*L*)/2 if a random orientation of the particle *L* (or *I*) axis in the beam plane is assumed (see **Figure 8**). Taking into account the linear relationships of axes dimensions with particle D_{CE} found in **Figure IV.7C** for all analyzed ash particles at Stromboli, D_{CE} can be equated on average to 0.92 (I+L)/2 with a high correlation (R^2 = 0.999). This relationship is used thereafter to find the circle-equivalent dimension of the disdrometer sized classes recording non-spherical ash particles. Hence, the lower detection limit of the disdrometer of 250 µm corresponds to 230 µm in circle-equivalent diameter.

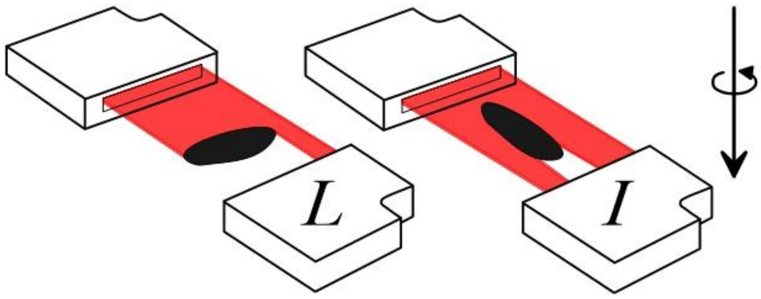

Figure 8: *Schematic representation of particle orientation when crossing the disdrometer laser beam. Assuming random rotating motion and no tumbling, particles may present a length, which is assumed to be equal to* (I+L)/2.

With increasing D_{CE}, the I/L ratio (*i.e.* the particle elongation of Bagheri & Bonadonna, 2016b) increases non-linearly from 0.66 for D_{CE} < 63 µm to 0.83 for D_{CE} > 710-1414 µm (**Figure 7D**). Particles tend to be more elongated with decreasing D_{CE}. This result supports the idea of an increasing proportion of particles passing through smaller sieves during manual sieving, as already suggested by **Figures 3** and **5**.

Figures 7A, **7B**, 7**C**, 7**D** and **Table 2** show the overall morphological similarity among all the ash samples (*i.e.* overlap in morphological parameter space) and the consistent variation of the morphological parameters as a function of size. However, there is an intrinsic heterogeneity existing inside each sample and each sieved fraction is characterized by: (i) the individual scattering of average values of C_v as a function of S_d (**Figure 7A**) and (ii) the increased spread of all shape parameter standard deviations (**Figures 7B**, **7C** and **7D**). This needs to be considered when interpreting disdrometer field measurements of falling ash.

In the next section, we use the G3's capability to measure individual particle shape parameters, in order to compare V_T measured in the field by the disdrometer, as a function of particle size, with existing V_T models.

4. Terminal settling velocities

4.1 Field measurements

The disdrometer recorded two ash fallout events on October 2 at 12:46 UTC (**Figure 9A**) and October 3 at 16:01 UTC (**Figure 9B**) totaling 355 and 2684 detected particles, respectively, which were also sampled from ground tarps (1246_roc and 1601_summit samples). Ash particles are detected in the first five size classes (*i.e.* 230 < D_{CE} < 804 μm) and the maximum number of particles (*i.e.* the mode of the PSD) occurs in the 345-460 μm class. Settling velocities ranges from 0.6 to 3.6 m s^{-1} and tends to increase with particle size, as tracked from their modal value across the size classes. For both events, modal V_T are comparable: particles of 230-345 μm show $1.2 < V_T < 1.6$ m s^{-1} and those of 345-460 μm (PSD mode) show $2 < V_T < 2.4$ m s^{-1}. Particles bigger than 574 μm show $V_T \leq 3.6$ m s^{-1} in **Figure 9A** and $1.6 < V_T < 2$ m s^{-1} in **Figure 9B,** and are present in a small amount (see PSD values in **Figures 2** and **5**). Despite its lower detection limit of 230 μm (in D_{CE}), the disdrometer was able to detect at least 75% and 94% (in vol. %) of the particles present in the 1601_summit and 1246_roc samples analyzed by the G3. In every size class, the spread of V_T around the modal value is remarkably wide. In the next two sections, we focus on results of V_T obtained with a representative sample with the highest collected mass (1601_summit).

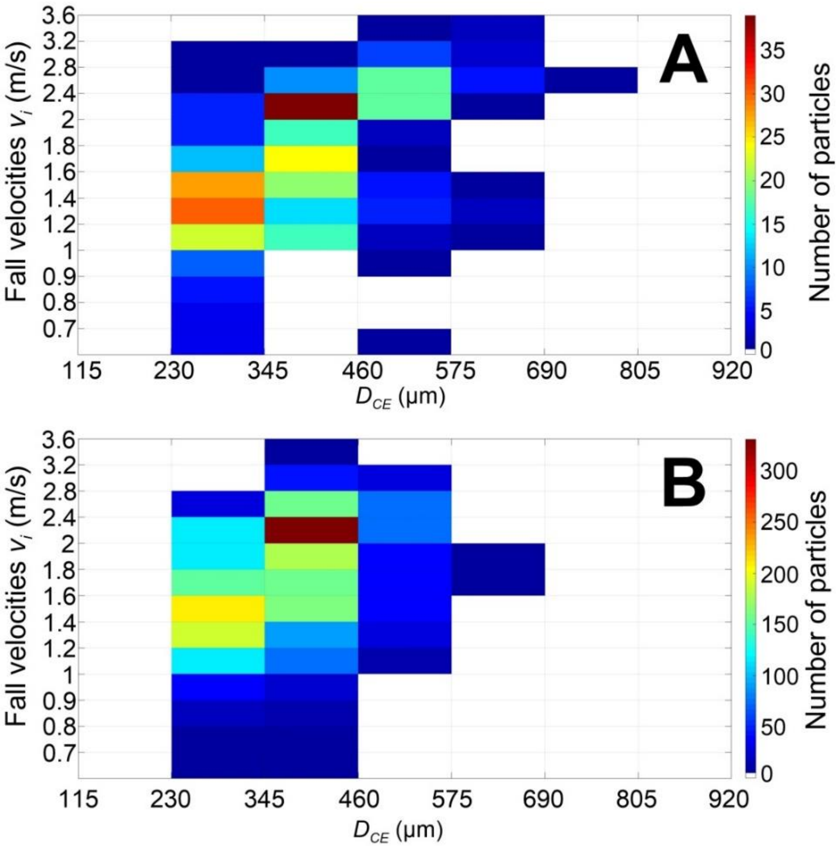

***Figure 9**: Settling velocity as a function of particle size classes measured by disdrometer during two ash fallout events at Stromboli. **A)** at 12:46 UTC (10/02/2015) and **B)** at 16:01 (10/03/2015). The color code represents the sum of the detected number of particles inside each class of velocities (y axis) and sizes in circle-equivalent diameter (D_{CE}, x axis).*

4.2 Laboratory experiments on ash settling velocity

V_T of dropped individual ash particles from the different sieved fractions is measured by the disdrometer under laboratory conditions of no wind. As expected, V_T distributions for each sieved fraction (**Figure 10A** and **10B**) are unimodal. The most frequently measured V_T increases with increasing D_{CE} from 0.95 m s^{-1} ± 0.05 m s^{-1} for 125-212 µm, to 3.8 m s^{-1} ± 0.1 m s^{-1} for 600-1000 µm (Black dashed line in **Figure 10A**). Nevertheless, the spread of V_T above and under the modal V_T values in each size class (grey dashed line in **Figure 10A**) highlights the aforementioned heterogeneity of PSDs and particle shapes shown by **Figures 3** and **Figure 7**, respectively, in each sieved fraction (**Figure 10D**). Moreover, the individual detected PSDs from the disdrometer are in broad agreement with the G3 PSDs, taking into account the ratio between D_{CE} and $(L+I)/2$ (**Figure 10C** and **10D**). Likewise, a comparison of the mode and adjacent values of V_T of each sieved fraction (**Figure 10B** and dashed lines in **Figure 10A**), or all measurements of V_T, shows broad agreement between values recorded in control experiments and in the field (blue and red histograms in **Figure 10A**, respectively). This highlights, in turn, the quality of the disdrometer data and the broad agreement between field and laboratory measurements. However, the distribution of field V_T of the 575-690 µm class appears to be bimodal: modal V_T measured in the lab matches the field mode at 3 m s^{-1} while most of the coarse particles in the field fell at lower V_T (mode at V_T = 1.9 m s^{-1}).

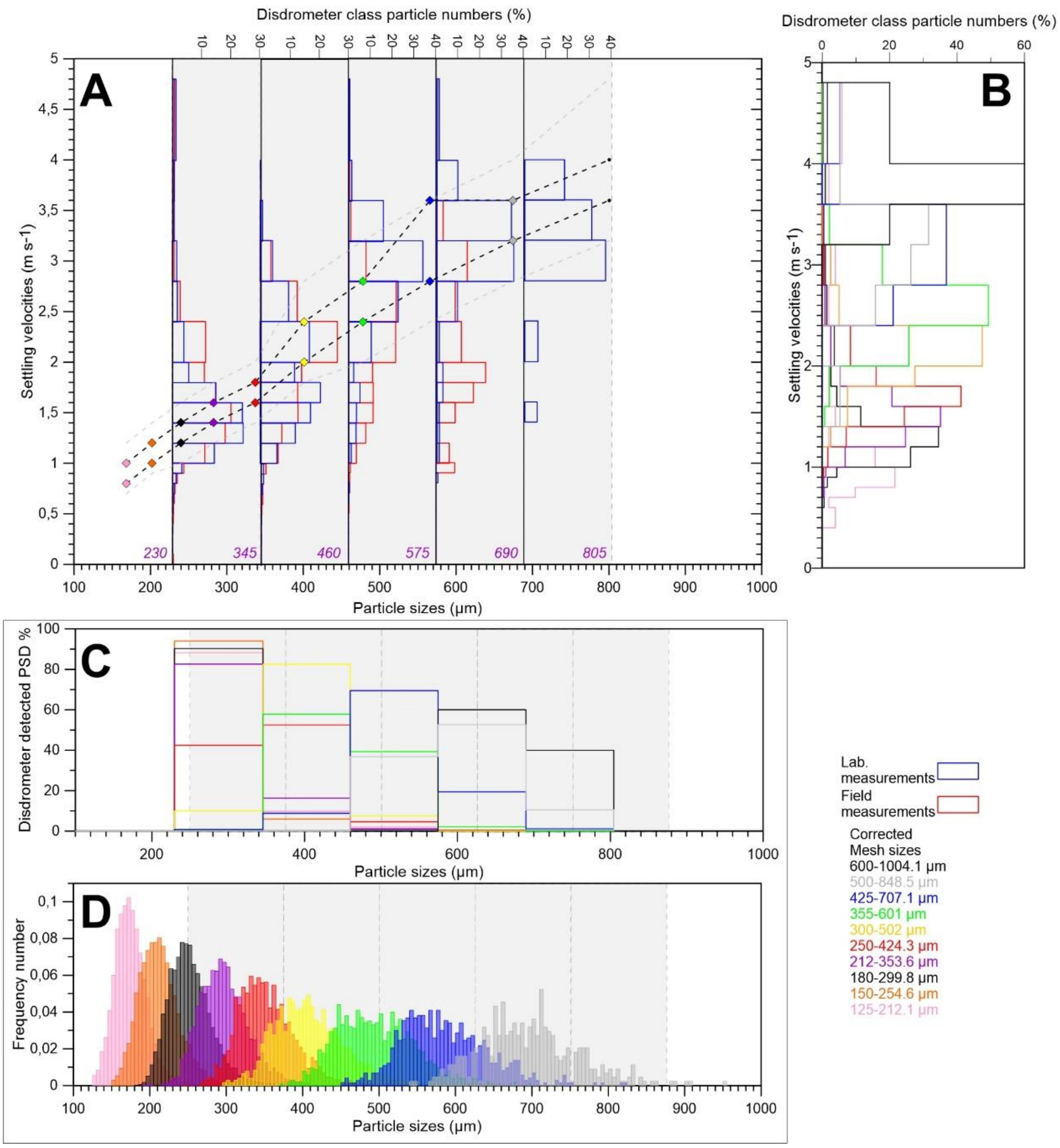

***Figure 10**: **A)** Settling velocities measured by disdrometer in laboratory conditions (blue histograms) and in the field (red histograms) for every sieved fraction from the 1601_summit sample. Dashed lines encompass the most frequently measured velocities (mode, bold black line) and adjacent classes (grey line). **B)** Histogram of settling velocities recorded by the disdrometer in each sieve class. **C)** Detected PSD (in percentage) and **D)** G3-derived PSDs (in frequency) of each sieve fraction.*

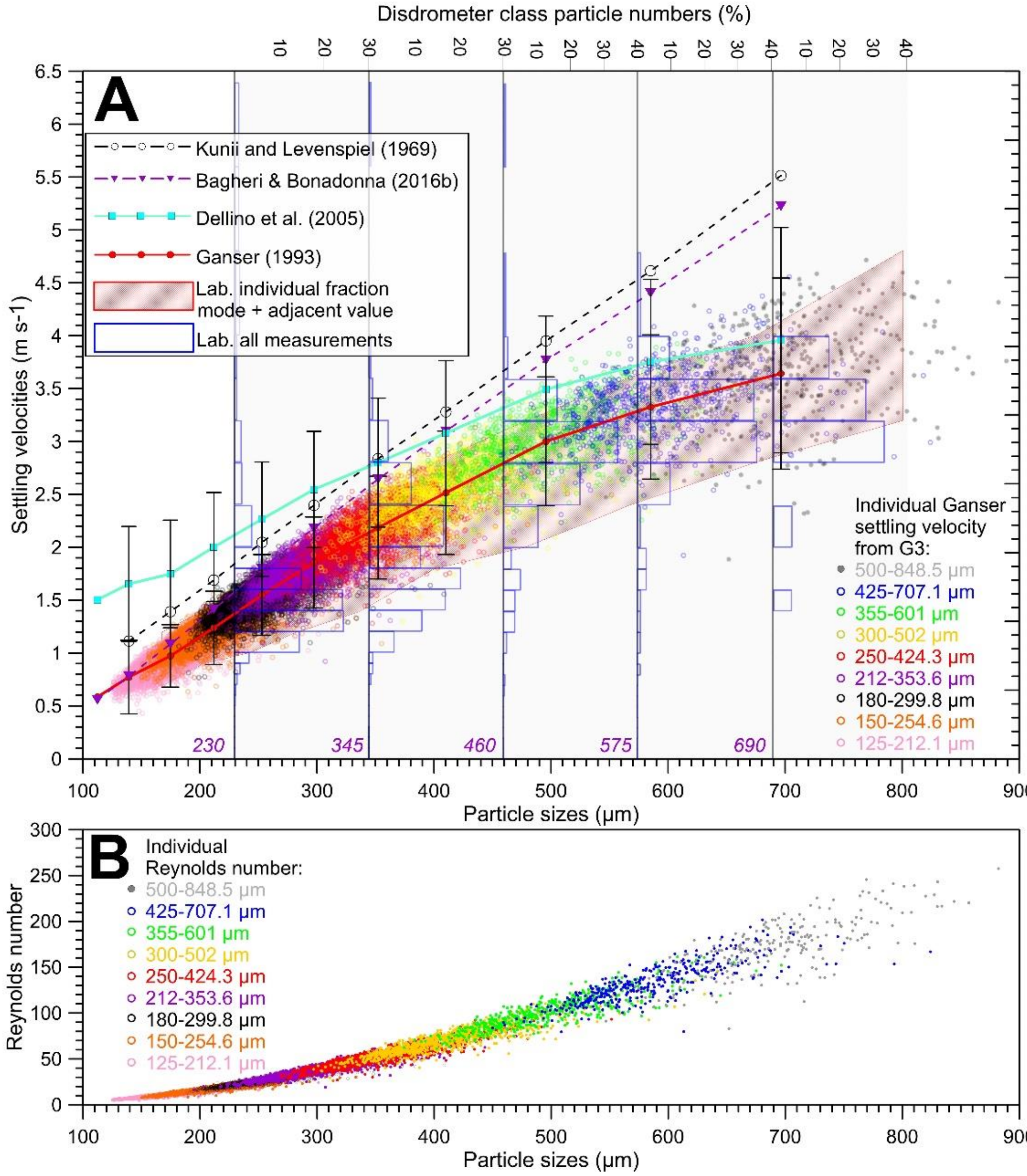

***Figure 11**: A) Average settling velocities measured by disdrometer in laboratory conditions (red area encompassing mode and adjacent velocity values, blue histograms for all measured velocities) and calculated with empirical models (curves) using the morphological parameters' average values obtained from the G3 optical analyses. Best match of the Ganser (1993) model (red curve) with the disdrometer data. V_T calculated with the Ganser (1993) model for all analyzed particles of the 1601_summit sample in each sieve fraction are displayed with colored dots. Error bars correspond to the standard error of the mean for every size class of particle V_T. **B)** Individual Reynolds number calculated with the Ganser (1993) drag equation as a function of all analyzed particle sizes of the 1601_summit sample.*

4.3 Empirical modeling

We compare 1601_summit ash V_T measured under laboratory conditions against the four empirical models described in **section 2** (**Figure 11A**). Using the average φ, D_{CE} values and densities found for each sieved fraction (**Appendix C**), we find that the Ganser model best describes the increase in V_T for particles with D_{CE} from 125 to more than 800 µm in our data. As shown in the preceding sections, the heterogeneity of particle shapes, sizes and densities is the cause of the spread of settling velocity measurements either in the field or under laboratory conditions. Therefore, we used the G3-inferred individual particle shape parameters to initialize the Ganser model.

5. Discussion

5.1 Empirical model validation

The combination of empirical models describing V_T of non-spherical particles permits identification of the effects of physical ash particle characteristics such as size, density and shape on the V_T calculation and also highlights the limits and strengths of each model. As described in Beckett *et al.* (2015), V_T empirical models are mainly sensitive to ash PSD, whereas their sensitivity to the shape and density is of lesser importance, but still relevant for precise V_T modeling. Knowing the PSDs of ash fallout samples at high size-resolution allows quantification of the sensitivity of such models to particle shape and density with a higher precision. For the models of Ganser (1993) and Bagheri & Bonadonna (2016b), the main parameter controlling V_T is the shape parameter used to calculate the drag coefficient. Ganser's model requires the particle sphericity φ, whereas the Bagheri & Bonadonna model requires 3-D particle measurements such as lengths of L, I and S axes. Because the short axis (S) is not measured by the G3 optical analysis in 2-D, we had to hypothesize S as equal to the intermediate (I) axis. This assumption tends to overestimate V_T in the Bagheri & Bonadonna model. Nevertheless, in order to obtain similar V_T values between both models, S must be between $0.4I$ and $0.1I$. Such S/I ratios, no matter the L values, would correspond to thin or tabular particle shapes, which do not characterize the average shape of our analyzed dense ash particles. Hence, the methodology and analyzed particles used in this study do not permit us to use the Bagheri & Bonadonna model for modeling terminal settling velocities.

There are two explanations for the better agreement between our measurements and the velocities of Ganser (1993). First, regarding the abundant presence of dense ash fragments with regular and rounded shapes (**Figures 7A**, 7**B**, 7**C** and **7D**), the sphericity φ of Riley *et al.* (2003)

appears to be the optimal parameter to describe our grain population among the 6 ash samples. Such a parameter is known to be well suited for the accuracy of Ganser's V_T equation (Alfano *et al.*, 2011).

Secondly, values of V_T calculated from empirical models depend on the accuracy of the shape factors used to determine the drag coefficient. φ is calculated from the particle area (*i.e.* linked to its shape) but also its perimeter, which strongly depends on the small scale particle roughness. For example, in Dioguardi *et al.* (2017), a 3-D sphericity is defined using X-ray microtomography. Their sphericity values are much lower ($\varphi < 0.434$) than those obtained by 2-D analyses owing to the high spatial resolution that takes into account the particle roughness at a very small scale. The G3 is less precise than X-ray microtomography for measuring small scale particle asperities, indicating that the variations of φ are mainly due to changes in particle shapes rather than in their roughness (Dioguardi *et al.*, 2018). Moreover, Strombolian ash particles have small-scale roughness as in the study of Ganser (1993). Taken together, these observations explain why, using our methodology, the best model describing V_T, measured by the disdrometer over the largest interval of ash sizes, is the Ganser model. Using the morphological parameters from our G3 optical analyses, **Equation 14** in Dellino *et al.* (2005) is thus valid for coarse ash and lapilli, which remain sparse at Stromboli. Indeed, **Equation 14** is established for a set of particles having a Reynolds Number > 60-100 (Dioguardi *et al.*, 2018), a range which corresponds to 5-10% of ash particles among the 1601_summit sample with D_{CE} larger than 360 to 560 μm (**Figure 11B**).

V_T calculated with the Ganser model for every analyzed particle for the 1246_roc and 1601_summit samples is in good agreement with ash V_T measured in the field (**Figures 12A** and **12B**) and under laboratory conditions. However, as observed in **Figures 9** and **10,** small V_T are also observed in the upper disdrometer classes above 460 μm in both contexts. Those V_T can be due to several effects: (i) the V_T being calculated from the crossing times of particles. Ash particles might not have fallen perpendicularly to the laser sheet, *i.e.* non-vertical trajectories, possibly due to the wind, causing longer crossing periods and thus lower V_T. (ii) As shown by Bagheri & Bonadonna (2016b), particles may fall with their longest axis perpendicular to their settling axis but may also oscillate and rotate according to this axis resulting in varying crossing times corresponding to one of the 3-D axes of the particles. It is unclear why any of these processes would have affected mainly coarser particles.

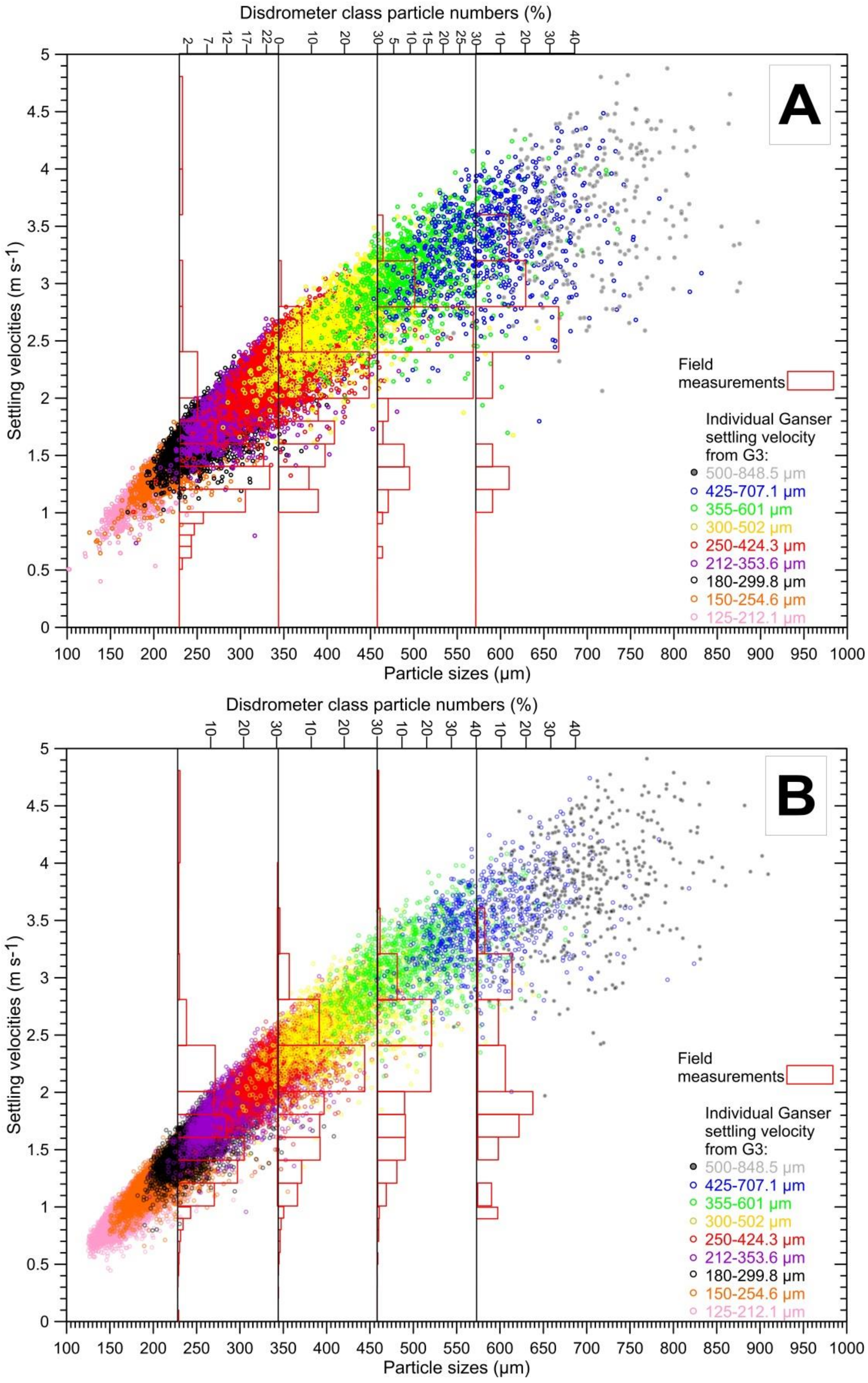

***Figure 12**: Individual particle V_T calculated with the model of Ganser (1993) based on sphericities (φ) and particle sizes measured by G3 in each sieved fraction (color code) for the October 2 2015 at 12:46 UTC **(A)** and October 3 2015 at 16:01 UTC **(B)** fallout events. Associated ash deposits, 1246_roc and 1601_summit samples respectively, were collected from ground tarps immediately after each fallout event. The distribution of disdrometer velocities measured in the field is shown in histograms for comparison.*

5.2 Application of particle shape and disdrometer measurements to radar retrievals

During our measurement campaign, a 3 millimeter-wave Doppler radar was used in addition to the disdrometer to record ash plumes dynamics and quantify ash concentrations (Donnadieu *et al.*, 2016). Inside a radar beam, when a continuously emitted electromagnetic wave encounters ash particles, its backscatter towards the radar induces a signal, the power of which is used to calculate a reflectivity factor Z. By assuming that the target PSD in the probed radar volume is composed of homogeneously distributed spherical ash particles with known diameter D (Sauvageot, 1992):

$$Z = \int_{D_{\min}}^{D_{\max}} N(D) D^6 dD.$$

(15)

Z characterizes the volcanic mixture remotely probed by the radar beam and directly reflects the particle volume concentration, however the strong contribution of spherical particle sizes (D^6) and lesser contribution of particle amounts ($N(D)$) of each size cannot be isolated without further constraints. One potential application of accurately characterizing volcanic particle sizes is to refine radar retrievals. Disdrometer measurements of the number of individually detected particles, their V_T and sizes allows estimation of radar reflectivity factors and associated ash concentrations. Thus, the coupling of radar and optical disdrometer methods, as implemented in meteorology (Marzano *et al.*, 2004; Maki *et al.*, 2005), will refine ash mass load retrievals from radar remote sensing of ash plumes and their fallout.

The methodology applied in this study to characterize volcanic particle shapes improves the interpretation of disdrometer outputs for a more accurate radar reflectivity estimation. The combination of disdrometer measurements of $v_i = V_T$ and number of detected particles is used to infer a particle number density per unit volume $N(D)$ (**Equation 4**), which is used, in turn, to automatically calculate Z from the measured sizes of particles detected by the disdrometer. Under the assumption that particles fall with their L and I axes in the beam plane (i.e. horizontal), the raw disdrometer reflectivity, Z_{disdro}, is calculated directly from the detected diameter, therefore assuming spherical particles, so that Z_{disdro} is biased for non-spherical particles depending on their orientation when crossing the beam. For example, the size of particles crossing the beam with their longest axis (L) normal to the detectors alignment are overestimated, and so is Z. Contrastingly, Z is underestimated when the intermediary axis is seen by the beam. From our morphological study, carried out statistically on a large number of ash particles, we conclude that the conversion of D_{CE} = 0.92 (L+I)/2 is appropriate (R^2 of 0.999 in **Figure 7C**) and can be used to constrain disdrometer reflectivities of Strombolian ash.

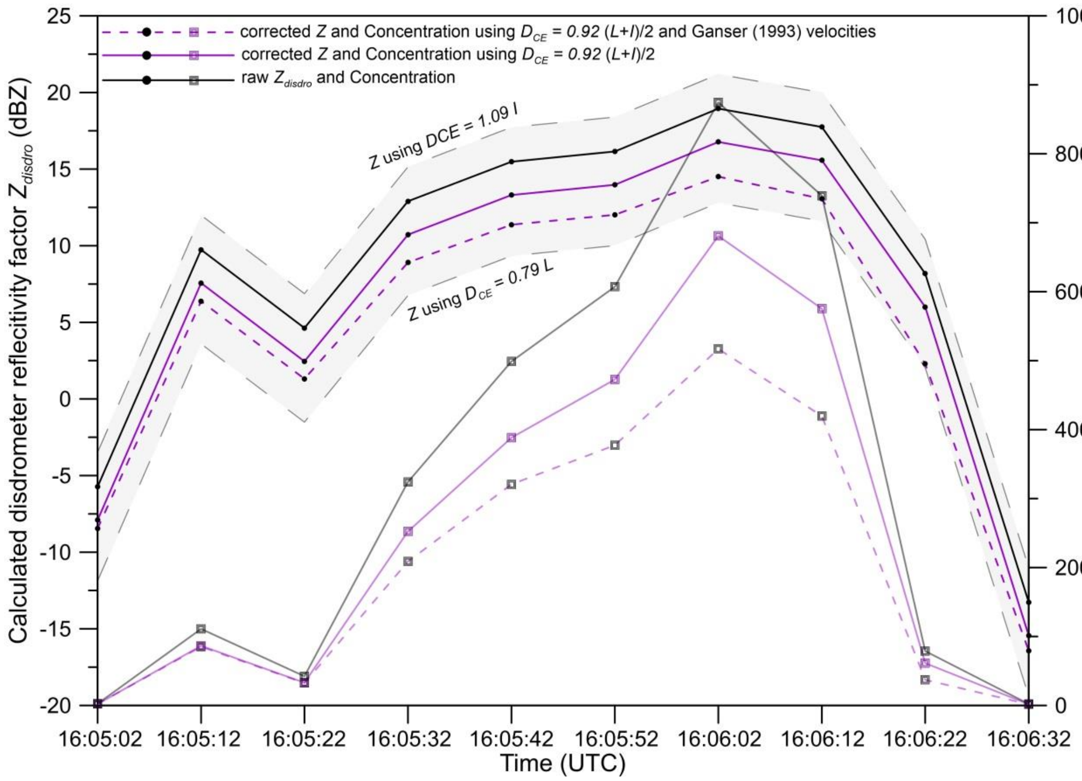

***Figure 13**: Disdrometer reflectivity factor (Z_{disdro}, dot lines) and ash concentration (line with squares) calculated from disdrometer measurements as a function of time during an ash fallout event on October 3 2015 (event 16:01 UTC corresponding to the sample 1601_summit). The black dot line corresponds to the raw Z_{disdro} calculated with no particle shape conversion, whereas the grey area represents the raw reflectivity if the disdrometer detected all particles respectively along their longest and intermediate axis. Purple line and purple dashed lines indicate Z and concentration values by correcting, respectively, only particle sizes in circle-equivalent diameter (D_{CE} inferred from G3 analyses), or both D_{CE} and settling velocities using the Ganser model (1993).*

Comparing Z_{disdro} with and without (i) conversions for circle-equivalent diameter and (ii) model-derived V_T (**Figure 13**) shows the respective influence of these two parameters (that are used to calculate $N_i(D_i)$ in **Equation 4** and **Equation 15**) on the reflectivities. Correcting the PSD by using the ratio (L+I)/2 shows a decrease of 2.18 dBZ in average (**Figure 13**). This highlights the necessity to physically characterize non-spherical particles, such as volcanic ash, and then to correct disdrometer data accordingly when comparing with reflectivities measured *in situ* inside the ash mixtures (*i.e.* plume and fallout).

Furthermore, the best fitting Ganser (1993) model V_T measured by the disdrometer in the field can be used to calculate V_T and correct for the data scattering, in particular the outlying low V_T of coarse ash measured in the field (**Figures 9** and **10**). This results in a further average difference of 1.8 dBZ compared to the PSD correction using the conversion of $(L+I)/2$, *i.e.* a total decrease of 4 dBZ using PSD and V_T correction with respect to reflectivities calculated from raw data.

Finally, detected ash concentration C_{ash} may be calculated using the following equation:

$$C_{ash} = \frac{\pi \rho_i}{6} \int_{D_{i\,\min}}^{D_{i\,\max}} N_i(D_i) D_i^3 dD_i \ . \tag{16}$$

As a result, disdrometer-derived ash concentrations span between 2.23 and 874.52 mg m^{-3} without any correction for diameters (**Figure 13**). Using the $(L+I)/2$ conversion leads to smaller ash concentrations to 1.73-680.79 mg m^{-3} (average difference of 22.155 ± 0.003%). Moreover, the use of Ganser's equation (1993) decreases conversion-derived and initial concentrations of 14.32% and 33.3%.

Despite the main dependence of ash reflectivity factors and concentrations on particle size (D^6 in **Equation 15** and D^3 in **Equation 16**), low velocities measured by the disdrometer in the field seem to have a non-negligible impact on the quantitative retrievals obtained from disdrometer retrievals.

Thus, as in meteorology, considering similar PSDs between the atmospheric volumes possibly probed by the radar and fallout measurements at ground level (Marzano *et al.*, 2004; Maki *et al.*, 2005), the disdrometer-inferred reflectivity factors provide a reasonable first-order quantification of ash concentrations inside volcanic ash plumes. The next step is to compare disdrometer-inferred reflectivity factors with reflectivity factors measured by radar inside the ash plumes and then estimate the spatial distribution of the ash mass load, one of the most crucial source term parameters.

5.3 Validation and limitation of disdrometer data

Despite a disdrometer lower detection limit of 230 µm in D_{CE} (*i.e.* only coarse ash is detected), the morpho-grainsizer G3 measurements and disdrometer measurements yield similar PSD modes. The low proportion of coarse ash larger than 690 µm detected by the disdrometer can be explained by the difference of spatial resolution between the instrument and the tarp used to sample the fallout (*i.e.* a laser sheet surface of 0.0054 m^2 compared to a 0.4 m^2

tarp). Indeed, the relatively low percentage of particles coarser than 575 μm (between 0.21 and 13.75% in **Figure 5**) can lead to an under-sampling of such sparse particles by the disdrometer.

The tests under laboratory conditions using empirical models validate the disdrometer V_T measurements in the field. However, field measurements show a high dispersion of V_T. With a modal value of 2.2 ± 0.2 m s^{-1}, measured V_T in the class 345-460 μm (**Figure 10**) range between 1 ± 0.1 m s^{-1} and 3 ± 0.2 m s^{-1}. Such a high variability is also seen with no-wind conditions in the laboratory (**Figures 10** and **11**). We attribute such variations to fluctuations in vertical wind and beam crossing trajectories, but also due to the high variability of particle shapes, sizes, and densities that lead to many possible combinations of interactions with the ambient fluid that can induce 3-D changes in particle rotation (Bagheri & Bonadonna, 2016b).

6. Conclusive remarks

This study presents an exhaustive characterization of the ash produced during explosions at Stromboli. We also perform an inter-comparison of empirical settling velocity models to validate terminal settling velocities measured by an optical disdrometer in the field.

The use of mechanical sieving and the morpho-grainsizer MORPHOLOGI G3 reveals the need to consider the geometrical influence of the sieve meshes in the case of non-spherical and rough ash particles. We propose the use of the lower mesh size and the diagonal of the upper mesh size of the mechanical sieve to constrain each PSD fraction.

We further propose a method to obtain a total PSD by combining the morpho-grainsizer high-resolution PSD with the weight percentages measured by the mechanical sieving. Our analyses reveal dense and homogenous ash particles in terms of textural and morphological roughness for a set of type 2 eruptions from proximal to medial distance (2 km) from the summit vents of Stromboli. The non-spherical ash particles sampled at Stromboli have their circle-equivalent diameter equal to 0.79 times their longest axis, 1.09 times their intermediate axis on average and 0.92 times their average 2-D dimension (L+I)/2. Moreover, we show that particle sphericity tends to slightly decrease with increasing D_{CE}. This observation may have strong implications for ash dispersion modeling, even in the case of moderate-sized eruptions. Indeed, the residence time of airborne ash particles has been shown to be highly dependent on their shapes, mostly for coarse ash with D_{CE} > 200 μm (Beckett *et al.*, 2015; Saxby *et al.*, 2018).

Disdrometer settling velocity measurements of sieved ash fractions under laboratory conditions are in broad agreement with the field settling velocities. This validates the volcanological application of the meteorology-designed OTT Parsivel^2 disdrometer for the detection and real-time recording of ash particle fallout size and settling velocities. Its limitations mainly concern the lower threshold in size measurements (230 microns in circle-equivalent diameter at Stromboli) and the width of each size class (*i.e.* around the 115 µm size class when used for ash measurements).

Empirical models used to calculate terminal settling velocities are highly dependent on the input shape parameters and their accuracy. Whereas the Bagheri & Bonadonna (2016b) and Dioguardi *et al.* (2017) models are based on high precision 3-D analyses of particles, the lower-resolved G3-derived sphericities from fast routine 2-D optical analyses are better matched to the Ganser model (1993). This is due to the fact that the output of our methodology more accurately reproduces the parameters used in Ganser (1993) to model terminal settling velocities.

Finally, the empirical results obtained with the Ganser model (1993) provide the best fit with the terminal settling velocities measured by the disdrometer and highlight the capability of such an instrument to operationally monitor volcanic ash sizes and their settling velocities with higher time resolution (10 s) than other in-situ methods. Despite underestimating coarse ash settling velocities, possibly due to particle interactions with the ambient fluid, our physical ash characterization emphasizes the need to constrain the size of both intermediate and long particle axes (*I* and *L*) and their settling velocities in order to calculate radar reflectivity factors. This underlines the important role of disdrometers in the field to constrain radar data for ash plume monitoring and mass load retrieval.

ACKNOWLEDGMENTS

We would like to acknowledge DPC members at Stromboli for their help during the measurement campaign, S. Valade (Univ. Firenze) for his precious help in the field, M. Ripepe for facilitating our work, and Mayor of Lipari for work authorization. All OPGC colleagues are deeply acknowledged for their work and enthusiasm in the field. Johanand Gilchrist is thanked for correcting the manuscript. We also thank Elisabetta Del Bello and an anonymous reviewer for their comments that significantly improved the manuscript. The optical disdrometer Parcivel^2 was purchased from the TerMEx-Mistrals INSU-CNRS program. This research was undertaken in the frame of EUROVOLC project and financed by the French Government Laboratory of Excellence initiative n°ANR-10-LABX-0006, the ANR STRAP, the Région Auvergne and the European Regional Development Fund. This is Laboratory of Excellence ClerVolc contribution number 331.

REFERENCES

Alfano, F., Bonadonna, C., Delmelle, P. & Costantini, L., 2011. Insights on tephra settling velocity from morphological observations. J. Volcanol. Geotherm. Res. 208, 86–98. doi:10.1016/j.volgeores.2011.09.013.

Andronico, D., Scollo, S., Cristaldi, A. & Lo Castro, M. D., 2014. Representivity of incompletely sampled fall deposits in estimating eruption source parameters: a test using the 12-13 January 2011 lava fountain deposit from Mt. Etna volcano, Italy. Bull. Volcanol. 76(10), 861. doi:10.1007/s00445-014-0861-3.

Bagheri, G. & Bonadonna, C., 2016a. Aerodynamics of Volcanic Particles: Characterization of Size, Shape and Settling Velocity. In: Mackie, S., Cashman, K., Ricketts, H., Rust, A., and Watson, M. (Eds.), Volcanic Ash, Elsevier 1, pp. 39–52. doi:10.1016/B978-0-08-100405-0.00005-7.

Bagheri, G. & Bonadonna, C., 2016b. On the drag of freely falling non-spherical particles. J. Powder Tech. 301, 526–544. doi:10.1016/j.powtec.2016.06.015.

Baxter, P.J., 1999. Cristobalite in Volcanic Ash of the Soufriere Hills Volcano, Montserrat, British West Indies. Science 283(5405), 1142–1145, doi:10.1126/science.283.5405.1142.

Beckett, F.M., Witham, C.S., Hort, M.C., Stevenson, J.A., Bonadonna, C. & Millington, S.C., 2015. Sensitivity of dispersion model forecasts of volcanic ash clouds to the physical characteristics of the particles. J. Geophys. Res. Atmos. 120, doi:10.1002/2015JD023609.

Bonadonna, C., Ernst, G. G. J. & Sparks, R. S. J., 1998. Thickness variations and volume estimates of tephra fall deposits: the importance of particle Reynolds number. J. Volcanol. Geotherm. Res. 81, 173–187.

Bonadonna, C., Genco, R., Gouhier, M., Pistolesi, M., Cioni, R., Alfano, F., Hoskuldsson, A. & Ripepe, M., 2011. Tephra sedimentation during the 2010 Eyjafjallajökull eruption (Iceland) from deposit, radar, and satellite observations. J. Geophys. Res. 116, B12202. doi:10.1029/2011JB008462.

Cashman, K. & Rust, A., 2016. Volcanic Ash: Generation and Spatial Variations. In: Mackie, S., Cashman, K., Ricketts, H., Rust, A., Watson, M. (Eds.), Volcanic Ash, Elsevier, pp. 5-21. doi:10.1016/B978-0-08-100405-0.00002-1.

Chien, S.F., 1994. Settling velocity of irregularly shaped particles. SPE Drill. Complet. 9, 281-288.

Cioni, R., Pistolesi, M., Bertagnini, A., Bonadonna, C., Hoskuldsson, A. & Scateni, B., 2014. Insights into the dynamics and evolution of the 2010 Eyjafjallajökull summit eruption (Iceland) provided by volcanic ash textures. Earth Planet. Sci. Lett. 394, 111–123.

Coltelli, M., Miraglia, L. & Scollo, S., 2008. Characterization of shape and terminal velocity of tephra particles erupted during the 2002 eruption of Etna volcano, Italy (2008). Bull. Volcanol. 70, 1103–1112, doi:10.1007/s00445-007-0192-8.

Corradini, S., Montopoli, M., Guerrieri, L., Ricci, M., Scollo, S., Merucci, L. Marzano, F.S., Pugnaghi, S., Prestifilippo, M., Ventress, L.J., Grainger, R.G., Carboni, E., Vulpiani, G. & Coltelli, M., 2016. A Multi-Sensor Approach for Volcanic Ash Cloud Retrieval and Eruption Characterization: The 23 November 2013 Etna Lava Fountain. Remote Sens. 8:58, doi:10.3390/rs8010058.

Del Bello, E., Taddeucci, J., Michieli Vitturi, M., Scarlato, P., Andronico, D., Scollo, S., Kueppers, U. & Ricci, T., 2017. Effect of particle volume fraction on the settling velocity of volcanic ash particles: insights from joint experimental and numerical simulations. Sci. Rep. 7, 39620, doi:10.1038/srep39620.

Dellino, P., Mele, D., Bonasia, R., Braia, G., La Volpe, L. & Sulpizio, R., 2005. The analysis of the influence of pumice shape on its terminal velocitiy. Geophys. Res. Lett. 32, L21306, doi:10.1029/2005GL023954.

Dioguardi, F. & Mele, D. (2015). A new shape dependent drag correlation formula for non-spherical rough particles. Experiments and results. Pow. Tech. 277, 222–230. doi:10.1016/j.powtec.2015.02.062.

Dioguardi, F., Mele, D., Dellino, P. & Dürig, T., 2017. The terminal velocity of volcanic particles with shape otained from 3D X-ray microtomography. J. Volcanol. Geotherm. Res. 329, 41–53, http://dx.doi.org/10.1016/j.volgeores.2016.11.013.

Dioguardi, F., Mele, D. & Dellino, P., 2018. A New One-Equation Model of Fluid Drag for Irregularly Shaped Particles Valid Over a Wide Range of Reynolds Number. J. Geophys. Res. 123. https://doi.org/10.1002/2017JB014926.

Donnadieu, F., Freret-Lorgeril, V., Delanoë, J., Vinson, J.P., Peyrin, F., Hervier, C., Caudoux, C. & Van Baelen, J., 2016. Multifrequency radar imaging of ash plumes: an experiment at Stromboli: EGU General Assembly Vienna, 23–28 April 2016.

Eychenne, J. & Le Pennec, J.L., 2012. Sigmoidal particle density distribution in a subplinian scoria fall deposit. Bull. Volcanol. 74, 2243–2249. doi:10.1007//s00445-011-0517-5.

Folk, R.L. & Ward, W.C. 1957. Brazos River bar: a study in the significance of grain size parameters. J. Geology 62, 3–26.

Ganser, G.H., 1993. A rational approach to drag prediction of spherical and non spherical particles. Powder Technol. 77(2), 143–152. http://dx.doi.org/10.1016/0032-5910(93)80051-B.

Gunn, R. & Kinzer, G., 1949. The Terminal Velocity of Fall for Water Droplets in Stagnant. Air. J. Meteorol. 6, 243–248.

Kunii, D.K. & Levenspiel, O., 1969. Fluidization engineering. Wiley, New York.

Lautze, N.C., Taddeucci, J., Andronico, D., Cannata, C., Tornetta, L., Scarlato, P., Houghton, B. & Lo Castro, M., 2011. SEM-based methods for the analysis of basaltic ash from weak explosive activity at Etna in 2006 and the 2007 eruptive crisis at Stromboli. Phys. Chem. Earth 45-46, 113–127, doi:10.1016/j.pce.2011.02.001.

Lautze, N., Taddeucci, J., Andronico, D., Houghton, B., Niemeijer, A. & Scarlato, P., 2013. Insights into explosion dynamics and the production of ash at Stromboli from samples collected in real-time, October 2009. In : Rose, W.I., Palma, J.L., Delgado Granados, H., and Varley, N. (Eds.), Understanding Open-Vent Volcanism and Related Hazards: Geological Society of America Special Paper 498, 125–139, doi:10.1130/2013.2498(08).

Leibrandt, S. & Le Pennec, J. L., 2015. Towards fast and routine analyses of volcanic ash morphometry for eruption surveillance applications. J. Volcanol. Geotherm. Res. 297, 11–27. doi:10.1016/j.jvolgeores.2015.03.014.

Liu, E.J., Cashman, K.V., Rust, A.C. & Gislason, S.R., 2015a. The role of bubbles in generating fine ash during hydromagmatic eruptions. Geology 43(3), 239–242, doi:10.1130/G36336.

Liu, E.J., Cashman, K.V. & Rust, A.C., 2015b. Optimising shape analysis to quantify volcanic ash morphology. GeoResJ 8, 14–30, http://dx.doi.org/10.1016/j.grj.2015.09.001.

Löffler-Mang, M. & Jürg, J., 2000. An Optical Disdrometer for Measuring Size and Velocity of Hydrometeors. J. Atm. Ocean. Tech. 17, 130–139.

Maki, M., Iwanami, K., Misumi, R., Park, S.G., Moriwaki, H., Maruyama, K.I., Watabe, I., Lee, D.I , Jang, M., Kim, H.K, Bringi, V.N. & Uyeda, H., 2005. Semi-operational rainfall observations with X-band mutli-parameter radar. J. Atmos. Sci. Lett. 6(1). https://doi.org/10.1002/asl.84.

Maki, M., Iguchi, M., Maesaka, T., Miwa, T., Tanada, T., Kozono, T., Momotani, T., Yamaji, A. & Kakimoto, I., 2016. Preliminary Results of Weather Radar Observations of Sakurajima Volcanic Smoke. J. Disaster. Res. 11(1), 15–30.

Marzano, F., Vulpiani, G. & Picciotti, E., 2004. Rain Field and Reflectivity Vertical Profile Reconstruction From C-Band Radar Volumetric Data. IEEE Trans. Geosci. Remot. Sens. 42(5). doi:10.1109/TGRS.2003.820313.

Marzano, F.S., Barbieri, S., Vulpiani, G. & Rose, W.I., 2006a. Volcanic ash cloud retrieval by ground-based microwave weather radar. IEEE Trans. Geosci. Remote Sens. 44, 3235–3246.

Marzano, F.S., Vulpiani, G. & Rose, W.I. (2006b). Microphysical Characterization of Microwave Radar Reflectivity Due to Volcanic Ash Clouds. IEEE Trans. Geosci. Remote Sens, 1–15. doi:10.1109/TGRS.2005.861010.

Patrick, M.R., Harris, A.J.L., Ripepe, M., Dehn, J., Rothery, D.A. & Calvari, S., 2007. Strombolian explosive styles and source conditions: Insights from thermal (FLIR) video. Bull. Volcanol. 69(7), 769–784, doi:10.1007/s00445-006-0107-0.

Pfeiffer, T., Costa, A. & Macedonio, G., 2005. A model for the numerical simulation of tephra fall deposits. J. Volcanol. Geotherm. Res. 140, 273–294. doi:10.1016/j.volgeores.2004.09.001.

Prata, A.J., 1989. Infrared radiative transfer calculations for volcanic ash clouds. Geophys. Res. Lett. 16(11), 1293–1296.

Prata, A.J. & Bernardo, C., 2009. Retrieval of volcanic ash particle size, mass and optical depth from a ground-based thermal infrared camera. J. Volcanol. Geophys. Res. 186, 91–107. doi:10.1016/j.jvolgeores.2009.02.007.

Prata, A.J. & Grant, I.F., 2001. Retrieval of microphysical and morphological properties of volcanic ash plumes from satellite data: application to Mt. Ruapehu, New Zealand. Quat. J. R. Meteorol Soc. 127(576), 2153–2179. https://doi.org/10.1002/qj.49712757615.

Riley, C.M., Rose, W.I. & Bluth, G.J.S., 2003. Quantitative shape measurements of distal volcanic ash. J. Geophys. Res. 108 (B10), 2504.

Sauvageot, H., 1992. Radar meteorology, Artech House, ISBN 0890063184, Boston.

Saxby, J. Beckett, F., Cashman, K., Rust, A. & Tennant, E. (2018). The impact of particle shape on fall velocity: Implications for volcanic ash dispersion modelling. *Journal of Volcanology and Geothermal Research*, 362:32–48. https://doi.org/10.1016/j.jvolgeores.2018.08.006.

Sparks, R.S.J., Bursik, M.I., Carey, S.N., Gilbert, J.S., Glaze, L.S., Sigurdsson, H. & Woods, A.W., 1997. Volcanic Plumes, Wiley, J., Chichester, England.

Tokay, A., Wolff, D.B. & Petersen, W.A., 2014. Evaluation of the New Version of the Laser-Optical Disdrometer, OTT Parsivel^2. J. Atm. Ocean. Tech. 31, 1276–1288. doi:10.1175/JTECH-D-13-00174.1.

Wilson, L. & Huang, T.C., 1979. The influence of shape on the atmospheric settling velocity of volcanic ash particles. Earth. Planet. Sci. Lett. 44, 311–324.

Wilson, T.M., Daly, M. & Johnston, D., 2009. Review of Impacts of Volcanic Ash on Electricity Distribution Systems, Broadcasting and Communication Networks, Auckland Engineering Lifelines Group Project AELG-19. Auckland Regional Council Technical Publication 051, April 2009.

Wilson, T.M., Stewart, C., Sword-Daniels, V., Leonard, G.S., Johnston, D.M., Cole, J.W., Wardman, J., Wilson, G. & Barnard, S.T., 2012. Volcanic ash impacts on critical infrastructure. J. Phys. Chem. Earth 45-46, 5–23, doi:10.1016/j.pce.2011.06.006.

Woods, A.W. & Bursik, M.I., 1991. Particle fallout, thermal disequilibrium and volcanic plumes. J. Volcanol. Geotherm. Res. 53, 559–570.

Appendix A: Mass (g) and mass percentage obtained for each sieved fraction for the six ash samples.

1/2 Φ	1601_summit		1246_roc		1530PL		1550_summit		1636_summit		1042-1252_roc	
Diameter (μm)	Mass (g)	wt%	Mass (g)	wt%	Mass (g)	wt%	Mass (g)	wt%	Mass (g)	wt%	Mass (g)	wt%
2000-2800											0,0299	0,4396
1400-2000	0,0099	0,0392									0,0426	0,6264
1000-1400	0,0055	0,0218	0,0064	0,1287							0,0111	0,1632
710-1000	0,0185	0,0733	0,0050	0,1006			0,0004	0,5891			0,0406	0,5970
500-710	0,6204	2,4590	0,1288	2,5909	0,0003	0,1157	0,0006	0,8837	0,0040	0,6416	0,0318	0,4676
355-500	4,4479	17,6295	1,2990	26,1305	0,0010	0,3855	0,0012	1,7673	0,0280	4,4915	0,0391	0,5749
250-355	7,9853	31,6503	2,3787	47,8496	0,0087	3,3539	0,0033	4,8601	0,1441	23,1152	0,2829	4,1597
180-250	5,5236	21,8932	0,7910	15,9117	0,0606	23,3616	0,0120	17,6730	0,2052	32,9163	1,2834	18,8710
125-180	3,6909	14,6291	0,1902	3,8260	0,1128	43,4850	0,0372	54,7865	0,1961	31,4565	2,1109	31,0385
90-125	1,6927	6,7091	0,0677	1,3618	0,0482	18,5813	0,0124	18,2622	0,0382	6,1277	1,4896	21,9030
63-90	0,7670	3,0401	0,0431	0,8670	0,0227	8,7510	0,0008	1,1782	0,0062	0,9945	0,8614	12,6660
0-63	0,4681	1,8553	0,0613	1,2331	0,0051	1,9661			0,0016	0,2567	0,5776	8,4930

1/4 Φ	1601_summit		1246_roc		1530PL		1550_summit		1636_summit		1042-1252_roc	
Diameter (μm)	Mass (g)	wt%	Mass (g)	wt%	Mass (g)	wt%	Mass (g)	wt%	Mass (g)	wt%	Mass (g)	wt%
2360-2800											0,0298	0,4501
2000-2360											0,0000	0,0000
1600-2000											0,0328	0,4954
1400-1600											0,0108	0,1631
1180-1400											0,0058	0,0876
1000-1180											0,0060	0,0906
850-1000											0,0209	0,3156
710-850							0,0004	0,7156			0,0171	0,2583
600-710	0,0726	0,3064	0,0173	0,3660	0,0000	0,0000	0,0000	0,0000	0,0016	0,2638	0,0090	0,1359
500-600	0,5189	2,1897	0,1034	2,1874	0,0001	0,0400	0,0003	0,5367	0,0022	0,3627	0,0171	0,2583
425-500	1,7265	7,2857	0,4670	9,8794	0,0004	0,1601	0,0004	0,7156	0,0052	0,8572	0,0168	0,2537
355-425	2,6035	10,9865	0,7508	15,8832	0,0003	0,1200	0,0003	0,5367	0,0240	3,9565	0,0242	0,3655
300-355	3,7705	15,9112	1,6416	34,7281	0,0027	1,0804	0,0013	2,3256	0,0699	11,5232	0,0865	1,3064
250-300	3,2857	13,8654	0,5719	12,0986	0,0047	1,8808	0,0016	2,8623	0,0537	8,8526	0,1236	1,8667
212-250	3,8763	16,3576	0,6160	13,0315	0,0213	8,5234	0,0043	7,6923	0,1360	22,4200	0,5249	7,9274
180-212	2,3582	9,9514	0,2050	4,3368	0,0414	16,5666	0,0081	14,4902	0,0893	14,7214	0,5555	8,3896
150-180	2,3027	9,7172	0,1390	2,9405	0,0703	28,1313	0,0159	28,4436	0,1316	21,6947	1,1451	17,2942
125-150	1,3902	5,8665	0,0480	1,0154	0,0416	16,6467	0,0132	23,6136	0,0571	9,4131	0,9691	14,6361
112-125	0,8370	3,5321	0,0238	0,5035	0,0198	7,9232	0,0040	7,1556	0,0186	3,0663	0,6154	9,2942
90-112	0,9551	4,0304	0,0286	0,6050	0,0234	9,3637	0,0051	9,1234	0,0117	1,9288	0,8304	12,5413
75-90					0,0122	4,8820	0,0008	1,4311	0,0038	0,6264	0,5278	7,9712
63-75					0,0075	3,0012	0,0001	0,1789	0,0011	0,1813	0,3712	5,6061
0-63							0,0001	0,1789	0,0008	0,1319	0,6815	10,2925

Appendix B: Disdrometer classification of settling velocities.

Class index	Settling velocity (m s^{-1})	Class spreading (m s^{-1})
1	0.05	0.1
2	0.15	0.1
3	0.25	0.1
4	0.35	0.1
5	0.45	0.1
6	0.55	0.1
7	0.65	0.1
8	0.75	0.1
9	0.85	0.1
10	0.95	0.1
11	1.1	0.2
12	1.3	0.2
13	1.5	0.2
14	1.7	0.2
15	1.9	0.2
16	2.2	0.4
17	2.6	0.4
18	3	0.4
19	3.4	0.4
20	3.8	0.4
21	4.4	0.8
22	5.2	0.8

Appendix C: Average circle equivalent diameters $\overline{D_{CE}}$, Sphericities $\overline{\varphi}$ and densities $\overline{\rho}$ found for the two summit samples: 1246_roc and 1601_summit.

1246_roc Corrected Sieved fraction (µm)	$\overline{D_{CE}}$ (µm)	Std. error	$\overline{\varphi}$	Std. error	$\overline{\rho}$ (kg m^{-3})
500-600	698.97	± 3.77	0.706	± 0.005	-
425-500	588.36	± 2.3	0.745	± 0.003	2645
355-425	506.01	± 1.73	0.765	± 0.002	2710
300-355	415.56	± 1.24	0.770	± 0.002	2737
250-300	355.28	± 0.68	0.780	± 0.001	2708
212-250	307.82	± 0.58	0.776	± 0.001	2782
180-212	262.74	± 0.42	0.777	± 0.001	2811
150-180	228.19	± 0.75	0.765	± 0.002	2811
125-150	185.86	± 0.80	0.763	± 0.003	2811
1601_summit Corrected Sieved fraction (µm)	$\overline{D_{CE}}$	Std. error	$\overline{\varphi}$	Std. error	$\overline{\rho}$ (kg m^{-3})
500-600	696.59	± 3.06	0.737	± 0.003	-
425-500	585.16	± 2.08	0.764	± 0.002	2683
355-425	495.67	± 1.59	0.777	± 0.002	2728
300-355	410.08	± 1.13	0.765	± 0.002	2743
250-300	352.31	± 0.73	0.759	± 0.001	2772
212-250	297.37	± 0.51	0.759	± 0.001	2774
180-212	252.94	± 0.42	0.744	± 0.001	2792
150-180	211.87	± 0.35	0.730	± 0.001	2737
125-150	174.65	± 0.23	0.714	± 0.001	2724